CENTRO DE INVESTIGACIONES
EN ÓPTICA, A.C.

Synthesis, Functionalization and Characterization of Metallic Nanoparticles and Their Interaction with HeLa Cell Cultures

A DISSERTATION SUBMITTED AS PARTIAL FULFILLMENT OF THE REQUIREMENTS FOR THE DEGREE OF DOCTOR IN SCIENCE (OPTICS) AT CENTRO DE INVESTIGACIONES EN ÓPTICA

Versión definitiva. Incluye cambios sugeridos por los revisores

Pablo Eduardo Cardoso Ávila

Vo.Bo. Advisor: Juan Luis Pichardo Molina 15-junio-2016

Junio 2016
León, Guanajuato, México

A mis padres, Mayte y Eduardo,

y a mi hermano Leonardo.

Abstract

The present thesis is focused in two main subjects; the photochemical and chemical synthesis of silver and gold nanoparticles (NPs) and their functionalization in order to study their interaction with cell cultures.

The techniques used for the characterization of nanomaterials are described; electronic microscopies for the evaluation of size and shape, UV-Vis spectroscopy for the optical characterization and Raman spectroscopy for the evaluation of the functionalization of the NPs.

The use of photochemical methods for the synthesis of silver NPs allowed us to have control over the size and morphologies of the NPs obtained; which is essential for several applications. The results will show an exhaustive study on the photochemical synthesis of silver NPs; power radiation, different reagents and temperature were analyzed as parameters and the optimal conditions for the photochemical synthesis of decahedral NPs were obtained. The extension of the photochemical synthesis of silver NPs by using two light sources is also presented; this allowed to tune the optical properties of the silver NPs in a wider range and to obtain a variety of morphologies. We believe that, with the use of different light sources, this photochemical method can be extended so that other morphologies and the optical properties of the NPs can be tuned in a wider range.

On the other hand, the functionalization of the NPs is necessary to control their in-

teraction with other materials; in the case of biological applications the surface chemistry plays an important role on how the biological samples behave in their presence. Finally, some preliminary results on the interaction of NPs and cell cultures are presented; the silver and gold NPs, synthesized in our lab, were functionalized expecting to reduce their toxicity in cell cultures. Our experiments were focused in the study of the toxicity of the NPs capping molecules. We find that with the capping molecules we propose in this work, there was no sign of toxicity in HeLa cell cultures. With the results obtained it is clear that these NPs have the potential to be used for photothermal therapies, as markers or in applications were the interaction of the NPs with live cells is necessary.

Resumen

La presente tésis esta enfocada en dos temas: la síntesis fotoquímica y química de nanopartículas (NPs) de plata y oro, y su funcionalización para estudiar su interacción con cultivos celulares.

Las técnicas usadas para la caracterización de nanomateriales son descritas; Microscopías electrónicas para la evaluación de tamaño y morfología, espectroscopía UV-Vis para la caracterización óptica y espectroscopía Raman para la evaluación de la funcionalización

El uso de métodos fotoquímicos en la síntesis de NPs de plata nos permitió tener control sobre el tamaño y su morfología; lo cual es escencial para diversas aplicaciones. Se realizó un estudio exhaustivo de la síntesis fotoquímica de NPs de plata; la potencia de la radiación, diversos reactivos y la temperatura de reacción fueron analizados como parametros y las condiciones optimas para la síntesis de NPs decaedrales fueron obtenidas. La extencion de la síntesis fotoquímica de NPs de plata al usar dos fuentes de iluminación también es presentada; esto permitió sintonizar las propiedades ópticas de las NPs en un amplio rango y obtener una variedad de morfologías. Creemos que, con el uso de diferentes fuentes de iluminación, este método fotoquímico puede ser extendido para que se obtengan otras morfologías y las propiedades ópticas sintonizadas en un rango aún más amplio.

Por otro lado, la funcionalización de las NPs es necesaria para controlar su interacción con otros materiales; en el caso de aplicaciones biomédicas la química de superficie tiene un rol muy importante en especial con materiales de origen biológicos. Finalmente, algunos resultados preliminares en la interacción de las NPs y cultivos celulares son presentados; las NPs de plata y oro, síntestizadas en nuestro laboratorio, fueron funcionalizadas esperando reducir su toxicidad hacia cultivos celulares. Nuestros estudios estuvieron enfocados en estudiar la toxicidad de las moléculas que recubrían las NPs. Encontramos que los recubrimientos que propusimos no muestran signos de toxicidad en cultivos de células HeLa. Con los resultados obtenidos es claro que estas NPs tiene potencial para ser utilizadas en terapias fototérmicas, como marcadores o en aplicaciones donde la interacción con células vivas es necesaria.

Agradecimientos

La presente Tesis es un esfuerzo en el cual, directa o indirectamente, participaron varias personas leyendo, opinando, corrigiendo y dando ánimo.

Quiero agradecer especialmente a mi asesor, el Dr. Juan Luis Pichardo Molina por todo su apoyo durante estos años. Sin su guía no hubiera sido posible realizar este trabajo.

A mi comité de seguimiento doctoral, los doctores Elder de la Rosa y Noé Alcalá Ochoa, por sus valiosos comentarios durante estos años y por la revisión de esta tesis. También a los Doctores Oracio Barbosa y Miguel Vargas por la revisón y sus comentarios para mejorar esta tesis.

A la Dra. Myrna Sabanero Lopez y a la M. en C. Liss Flores Villavicencio, de la Universidad de Guanajuato, por su valioso apoyo en las pruebas biológicas sobre la interacción de las NPs en cultivos celulares.

A mis compañeros de laboratorio Monserrat, Yenny, Rigo y Pablo por su ayuda y por hacer de ese espacio un lugar agradable donde trabajar.

Al GPOM y sus miembros, los comentarios que recibí durante mi pertenencia a este grupo ayudaron bastante a dar forma al proyecto doctoral.

Al Centro de Investigaciones en Óptica por brindarme un espacio donde crecer académicamente y como persona. A todos los empleados del CIO, pero especialmente a los ingenieros Ricardo Valdivia y Martin Olmos, a Christian Albor del laboratorio de microscopía electronica y a los técnicos del taller mecánico Chuy Ortiz, Marco Troncoso y Luis Martínez.

A Claudia Elias Alfaro de la UASLP por su ayuda en la obtencion de imágenes de microscopía electronica.

Finalmente al CONACyT por el apoyo brindado mediante la beca doctoral.

Contents

List of Figures

List of Tables

CHAPTER 1

Introduction

Noble-metal nanoparticles (NPs) have received considerable attention over the last two decades due to their remarkable physical and chemical properties. When a metal Nanoparticle (NP) is exposed to light, the oscillating electromagnetic field of the light induces a collective coherent oscillation of the free electrons in the metal. The amplitude of the oscillation reaches maximum at a specific frequency, called localized surface plasmon resonance (LSPR) [1, 2]. The LSPR band is stronger for nanoparticles of noble metals, mainly for Au and Ag than other metals [3]. In general, gold and silver NPs exhibit a LSPR bands in the visible range, but in the case of gold NPs the plasmon band can also be tuned to the near infrared region [4]; just by changing their size, shape or local environment [5–8].

The potential applications of metallic NPs are full related with their optical and chemical properties. In the last decades metal nanoparticles like spheres, cubes, concave cube , nanorods, branches, decahedrons, octahedrons and other morphologies has been produced by chemical, thermal, electrochemical or photochemical syntheses in aqueous

solutions and other solvents [4, 9–16]. One of the most popular procedures for the synthesis of silver and gold nanoparticles is based on the use of sodium citrate, also known as Turkevich's method [17–20]. Several authors proposed different modifications to improve the synthesis of sodium citrate to gain better control of the nanoparticle (NP) size and morphology.

Another very popular method for the synthesis of gold NPs is based in the use of sodium borohydride, which acts as a reducer, for the formation of very stable and monodisperse spherical GNPs. It is also very common to use this $NaBH_4$ reduced GNPs as seeds for the formation of more complex morphologies. Seed particles are synthesized via the reduction of tetrachloroauric acid ($HAuCl_4$) by sodium borohydride ($NaBH_4$) in the presence of a stabilizing agent, commonly the surfactant cetyltrimethylammonium bromide (CTAB), though cetylrimethylammonium chloride(CTAC) and sodium citrate have also been used [21]. In order to control the shape, these seed NPs are transferred to a growth solution, which contains at minimum a surfactant, a source of Au ions, and a weak reducing agent [4, 15, 22–24]. In this second growth step, a weak reducing agent is chosen to prevent additional nucleation and to favor growth onto the preformed seeds, as well as to slow particle growth enough to allow for control of nanoparticle shape through the addition of shape-directing additives [21]. With this seed growth approach morphologies such as rods, triangular nanoprisms, cubes and octahedra can be easily obtained

On the other hand, there are several methods used to produce different faceted morphologies of Ag NPs; for example, Ledwith et al.[25] used silver seeds to produce triangular platelets of different sizes by controlling the concentration of sodium citrate as well as the temperature of the synthesis. Dong et al.[26] showed that controlling the pH of the reaction solution permits the control of the size and morphology of silver nanoparticles. Dong et al.[27], also reported the stepwise reduction of silver nitrate with sodium borohydride and trisodium citrate in an ice bath for 30 min, after which they heated the solution at 70^{o}C to trigger the remaining silver nitrate to obtain triangular silver

nanoprisms. Even when the thermal methods are the most straightforward in producing NPs, they produce a broad size distribution of NPs due to the use of high temperatures and strong reducing agents. As an alternative, photochemical methods have been developed for the synthesis of different morphologies [28, 29], e.g., spheres [30–32], decahedra [33–38], prisms [37–40], rods [41], pentagonal rods [42], disks [43, 44], and so forth.

In a pioneering work by Jin et al.[39], spherical silver nanoparticles (SS-NPs) were prepared by injection of sodium borohydride as a reducing agent into a solution containing silver nitrate and trisodium citrate; a conventional fluorescent light was used to irradiate the SS-NPs, and over 100 hours of light exposure were required to complete the photochemical reaction, converting spherical nanoparticles to nanoprisms. In a similar reaction, Maillard et al.[43] 457nm line of an Argon ion laser to produce prisms and disks; in a second step, these particles were transferred to a regrowth solution and two different wavelengths of the laser, 457 and 514nm, were used to produce a red-shift of the plasmon band to 540 and 585nm, respectively. Machulek et al.[45] used silver seeds deoxygenated by nitrogen bubbling to fabricate silver nanoprisms in an aqueous polyvinylpyrrolidone (PVP) solution followed by the photochemical synthesis under visible light irradiation. Using light irradiation out of resonance with the plasmon peak of the nanoparticle seeds, Rocha et al.[46] reported the photochemical synthesis of silver nanotriangles in an aqueous solution of sodium citrate and bis(p-sulphonatophenyl-phenylphosphine dehydrate dipotassium). Zheng et al.[28] proposed the use of Argon-ion laser lines at 514.5, 501.0, 488.0, 476.5 and 457.9nm to show the potential of the photochemical synthesis in controlling the nanoparticles size and morphology when the precursor solutions were prepared by a classical method [47]. The first three laser lines produce disc and triangular plates, while the last two lines produce decahedrons with low yield. On the other hand, efficiencies above 90% on the morphological selectivity of decahedral NPs were obtained by using a metal halide lamp as a light source and an aqueous silver nitrate solution with sodium borohydride in the presence of polyvinylpyrrolidone (PVP) and citrate as stabilizers, and arginine as a photochemical promoter, [33]. Additionally, the size of the NPs

was controlled using the previously prepared decahedral NPs by means of a multi-step re-growth process, resulting in sizes ranging from 35 to 123nm, which tuned the plasmon band from 455 to 570nm. One of the latest related studies was conducted by Stamplecoskie and Scaiano[29], who proposed a facile method to prepare silver nanoparticles of various sizes and morphologies using I2959 as a photochemical reductant, irradiating the precursor solution with a UV lamp for several minutes, and subsequently irradiating the solution with light-emitting diodes (LEDs) at different wavelengths. They were able to produce spherical, decahedron, hexagonal, triangular and rod silver nanoparticles using the low-power radiation of inexpensive light sources. Photochemical processing seems to offer good size and morphology control through the selection of appropriate surfactants, photocatalytic molecules and wavelengths of light. Combining the multi-step re-growth and the use of LEDs of different wavelengths, Lu et al.[34] obtained decahedral nanoparticles in sizes ranging from 28 to 67nm and tuned the plasmon band from 489 to 590nm. According to the authors, when the LED wavelength matches the LSPR of silver decahedral seeds, the formation of nanoprisms and nanoplates can be drastically suppressed, improving the uniformity of the desired nanostructures.

While many authors have reported studies utilizing the photochemical method, several questions remain regarding the role of some important parameters that control the photochemical synthesis.

The photochemical transformation is a simple and novel method to produce metallic NPs with different morphologies, the plasmon band can be tuned in a wide range of the visible spectrum, and their potential uses are also very wide, from sensors to biomedicine. But before nanoparticles can be used in any application their surface modifications always is recommended, this process is know as functionalization. By selecting the appropriated chemical species in the surface of the NPs it is possible to induce the interaction with other materials or with other nanoparticles. Functionalization is important because most of the optical properties of the metallic NPs are surface and distance dependent; in biological applications the functionalization or surface coating of the NPs plays a principal role

in the interaction of these materials and the biological systems. In the last decade gold nanoparticles have been used in innumerable biological tests with strong promising results in diagnosis, bioimaging, therapies, and to regulate release of drug [48–51]. However, many questions arise about of their safety use, but still not defined answers have been obtained. Toxicity evaluation of NPs is essential before any possible application, but actually nanoparticles of many classes can be found not only in experimental labs, but also in many commercial products. Related with it, the main problem with the use of NPs is that little information is available on their safety, because most works have been focused in showing the potential application of these materials. A few researches are worried about on their consequences, maybe because the evaluation of toxicity is difficult, it requires an exhaustive and long time consuming work, such as the analysis of many parameters that can be condensed in factors like physicochemical properties and the environmental conditions. For gold NPs (GNPs) toxicity, these parameters may vary according to size, roughness, form, aggregation state, coating, etc., making it difficult to provide a general result [52–56]. Nevertheless, some works have been trying to elucidate which are the main toxic factors. NPs geometry is an import factor in the toxicity evaluation and different works have been reported (nanospheres, nanorods, nanocubes and nanobranched particles), but still there is not conclusive result because coatings and molar concentration also need to be considered [22, 57]. For example sodium citrate and CTAB were two of the first tested coatings in gold nanoparticles [58]. Although the results showed a relative high degree of toxicity for both surfactants when they are used at high concentrations, in fact CTAB showed to be more toxic. New coatings have been tested improving the biocompatibility and reducing significantly the toxicity of them: ionic, anionic, zwitterionic, proteins, amino acids and synthetic polymers have been used to diminish the toxicity of NPs [59–63].

Motivation: The potential applications of metallic NPs are full related with their morphology and optical properties, so it is necessary to develop fabrication methods that allow to control these properties. In this work I wanted to explore the potential of the

photochemical methods to gain a better control on these properties when compared to the pure chemical methods. On the other hand, most of the synthetic methods make use of surfactants that are reported to be toxic under certain circumstances. Since I wanted to use these NPs in some biological applications, I wanted to explore their interaction and toxicity on cell cultures before to proceed to further experiments. The ultimate goal was to design and fabricate NPs for biomedical applications, in particular I was interested in photothermal therapy, so it is necessary to control the plasmon resonant band and to have non toxic NPs.

Objective: The objective of this thesis is to study the potential capabilities of the photochemical methods as way of getting control in the synthesis of silver NPs and to understand the NPs functionalization process and its effect when the NPs interact with HeLa cell cultures.

Thesis organization: This thesis describes the photochemical synthesis of silver NPs and the functionalization of both silver and gold NPs in order to study their interaction with cell cultures and to evaluate their cytotoxicity. The techniques used for the characterization of nanomaterials are described in Chapter 2; electronic microscopies for the evaluation of size and shape, UV-Vis spectroscopy for the optical characterization and Raman spectroscopy for the evaluation of the functionalization. In Chapter 3, an exhaustive study on the photochemical synthesis of silver NPs is shown; power radiation, different reagents and temperature were analyzed as parameters and the optimal conditions for the photochemical synthesis of decahedral NPs were obtained. The extension of the photochemical synthesis of silver NPs is explored in Chapter 4; here, the study of the photochemical synthesis was carried out by using two light sources, which allowed to tune the optical properties of the silver NPs in a wider range and to obtain a variety of morphologies. Next, the silver and gold NPs were functionalized, details on this can be found in Chapter 5. Decahedral NPs were functionalized as described in Section 5.1 expecting to reduce the silver cytotoxicity. Finally, Section 5.2 presents the functionalization gold nanoparticles and the introductory results on the biocompatibility

in cell cultures. These experiments had the objective to study the cytotoxicity of the nanoparticles capping molecules. In Chapter 6, the general conclusions of this thesis are presented along with some perspectives for this work.

CHAPTER 2

Techniques

Nanotechnology is a promising field which involve the fabrication and applications of materials that are in the nanometric range. The interest in this kind of materials is because it is known that when some materials are brought to nanometric dimensions, their chemical and physical properties are different to those of the bulk material, and this can have a huge impact in diverse technological applications. The fabrication of nanomaterials can be performed with a wide variety of methods (Chemical, electrical, optical and mechanical among others). The characterization techniques applied to the nanomaterials give information about the morphology, chemical composition, mechanical, optical and thermal properties, among others. The characterization techniques used in this thesis will be described giving a general overview of its fundamentals and its application to the characterization of nanomaterials. More in-deep information on these techniques can be found elsewhere.

2.1 Electronic Microscopy

The resolution of an optical imaging system can be limited by factors such as imperfections in the lenses or misalignment. However, there is a fundamental maximum to the resolution of any optical system which is due to diffraction. An optical system with the ability to produce images with angular resolution as good as the instrument's theoretical limit is said to be diffraction limited [64].

The observation of small structures with microscopes is limited by the Abbe diffraction limit. In 1873, Ernst Abbe found that light with wavelength λ, traveling in a medium with refractive index n and converging to a spot with angle θ will make a spot with radius [65]

$$d = \frac{\lambda}{2nsin\theta} \tag{2.1}$$

The denominator $nsin\theta$ is called the numerical aperture (NA) and can reach about 1.4–1.6 in modern optics. Considering green light around 500nm and a NA of 1, the Abbe limit is roughly $d = \lambda/2 = 250$nm (0.25μm), which is small compared to most biological cells (1 to 100μm), but large compared to viruses (100nm), nanostructures (<100nm), proteins (10nm) and smaller molecules (1nm). Therefore, in order to visualize structures in the nanometric scale it is necessary to use another type of microscopy.

In the other hand, Louis de Broigle proposed in 1924, that just as light has both wave-like and particle-like properties, electrons also have wave-like properties. The wavelength, λ, associated with an electron is related to its momentum, p, through the Planck constant, h:

$$\lambda = \frac{h}{p} \tag{2.2}$$

So, if an accelerated electron is used instead of visible light, the resolution of a microscope can be enhanced. For example, an electron at an energy of 10keV has a "de Broigle"' wavelength of 0.01nm, allowing the electron microscope to achieve high resolution images than an optical one.

In 1931, Ernst Ruska and Max Knoll constructed the first prototype of a transmission

electron microscope, capable of 400x power magnification. In 1937, Manfred von Ardenne pioneered the scanning electron microscope (SEM). Siemens produced the first commercial transmission electron microscope (TEM) in 1939. Although contemporary electron microscopes are capable of two million-power magnification, as scientific instruments, they remain based upon Ruska's prototype.

2.1.1 Transmission Electronic Microscopy

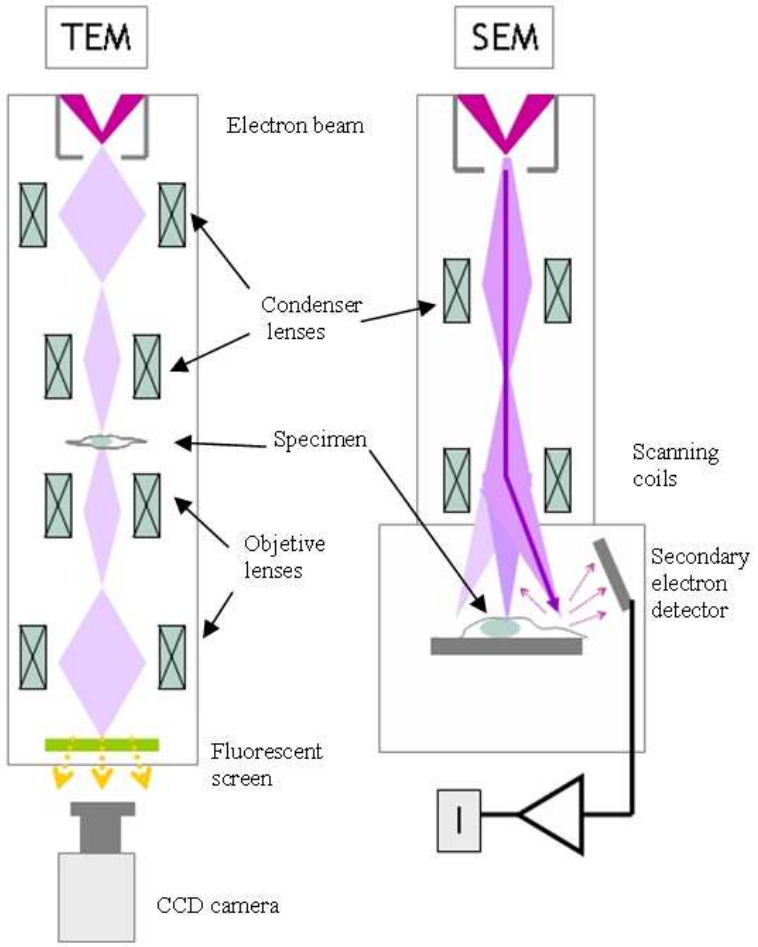

Figure 2.1.1: Schematics for the transmission and scanning electron microscopes.

The transmission electron microscope (TEM) uses a high voltage electron beam to create an image (Fig. 2.1.1). A tungsten filament serves as electron source. The electron beam is accelerated by an anode, typically around +100keV with respect to the cathode, focused by electromagnetic lenses and transmitted through the specimen. The specimen is prepared in a way that is in part transparent to electrons and in part scatters them out of the beam. When the electron beam is transmitted through the specimen it carries information about the sample which is then magnified by the objective lens system of the microscope generating the image. The image may be viewed by projecting the magnified electron image onto a fluorescent viewing screen coated with a phosphor. The image can be photographically recorded by exposing a photographic film or plate directly to the electron beam, or a high-resolution phosphor may be coupled by means of a lens optical system or a fiber optic light-guide to the sensor of a CCD camera, then the image detected by the CCD may be displayed on a monitor or computer.

2.1.2 Scanning Electronic Microscopy

The Scanning electronic microscope (SEM) produces images by scanning the specimen with a focused electron beam. When the electron beam interacts with the specimen, it loses energy by a variety of mechanisms, such as heat, emission of low-energy secondary electrons and high-energy back-scattered electrons, light emission or X-ray emission. All these mechanisms can provide information about the properties of the specimen surface, such as its topography and composition. The image displayed by a SEM shows the intensity variation of any of these signals. The conventional imaging mode in most SEM is produced by secondary electrons. Because the SEM relies on surface processes, it is able to image bulk samples up to many centimeters in size and has a great depth of field, and so can produce images that are good representations of the three-dimensional shape of the sample (Fig. 2.1.1).

2.2 Raman Spectroscopy

In 1928, Raman and Krishan discovered the inelastic scattering of light previously predicted by Smekal[66]. Raman spectroscopy is a spectroscopic technique used to observe vibrational and rotational modes in a system. Raman spectroscopy provides a fingerprint spectrum by which molecules can be identified; this is why is commonly used in chemistry, since vibrational information is specific to the chemical bonds and symmetry of molecules. In simple words, the Raman effect is a scattering phenomenon which relates the vibrational frequencies of molecules with the energy differences between the incident and scattered light by these molecules.

When a molecule interacts with an EM field, the energy transfer from the EM field to the molecule can only happen when the Bhor's frequency condition is satisfied:

$$\Delta E = E_2 - E_1 = h\nu = h\frac{c}{\lambda} = hc\overline{\nu} \tag{2.3}$$

where ΔE is the energy difference between two quantized states, E_2 and E_1 are the energies of the excited and base states respectively, h is the Planck's constant ($6.62\text{x}10^{-34}$J·s), c is the speed of light, λ is the wavelength and $\overline{\nu}$ is the wavenumber. Then a transition of $1cm^{-1}$ is equivalent to:

$$\Delta E = (6.62x10^{-34}J \cdot s)(3x10^{10}cm/s)(1cm^{-1}) = 1.99x10^{-23}J \tag{2.4}$$

In the Raman spectroscopy the sample is irradiated by intense lasers in the UV, visible and NIR regions. The collected light is composed by Rayleigh and Raman scattered light. Rayleigh light has the same frequency as the incident light and is the most probable event; the scattered intensity is ca. 10^{-3} less than that of the original incident radiation [67]. The Raman light, which is very weak (10^{-5} of the incident beam intensity), has frequencies $\nu_0 \pm \nu_m$, where ν_m is a vibrational frequency of a determined molecule. The frequencies $\nu_0 - \nu_m$ y $\nu_0 + \nu_m$ are known as the Stokes and anti-Stokes lines. In Raman spectroscopy, the vibrational frequency of the molecule ν_m is measured as a shift from

the frequency of the incident light ν_0.

According to the classical theory, Raman scattering can be explained as follows: The intensity of the electric field E of an EM wave varies in time as:

$$E = E_0 \cos(2\pi\nu_0 t) \tag{2.5}$$

where E_0 is the vibrational amplitude and ν_0 is the frequency of the light from the laser. If a diatomic molecule is irradiated by this light, a dipolar moment P is induced:

$$P = \alpha E = \alpha E_0 \cos(2\pi\nu_0 t) \tag{2.6}$$

where α is a constant called polarizability. If the molecule is vibrating with a frequency ν_m, the nuclear displacement q:

$$q = q_0 \cos(2\pi\nu_m t) \tag{2.7}$$

where q_0 is the vibrational amplitude. For a small amplitude, α is a linear function of q:

$$\alpha = \alpha_0 + \left(\frac{\partial\alpha}{\partial q}\right)_0 q_0 + ... \tag{2.8}$$

α_0 is the polarizability at the equilibrium position and $(\partial\alpha/\partial q)$ is the rate of change of α with respect to the change in q evaluated in the equilibrium.

By combining the eqs. 2.6, 2.7 and 2.8, we get:

$$
\begin{aligned}
P &= \alpha E_0 \cos(2\pi\nu_0 t) \\
&= \alpha_0 E_0 \cos(2\pi\nu_0 t) + \left(\frac{\partial\alpha}{\partial q}\right)_0 q E_0 \cos(2\pi\nu_0 t) \\
&= \alpha_0 E_0 \cos(2\pi\nu_0 t) + \left(\frac{\partial\alpha}{\partial q}\right)_0 q_0 E_0 \cos(2\pi\nu_0 t)\cos(2\pi\nu_m t) \\
&= \alpha_0 E_0 cos(2\pi\nu_0 t) \\
&+ \frac{1}{2}\left(\frac{\partial\alpha}{\partial q}\right)_0 q_0 E_0 \left[\cos(2\pi\left\{\nu_0+\nu_m\right\}t) + \cos(2\pi\left\{\nu_0-\nu_m\right\}t)\right]
\end{aligned}
\tag{2.9}
$$

where the first term corresponds to a dipole emitting at the frequency ν_0, this means Rayleigh scattering. Meanwhile, the second term corresponds to the Raman scattering of frequency $\nu_0 + \nu_m$ (anti-Stokes) and $\nu_0 - \nu_m$ (Stokes).

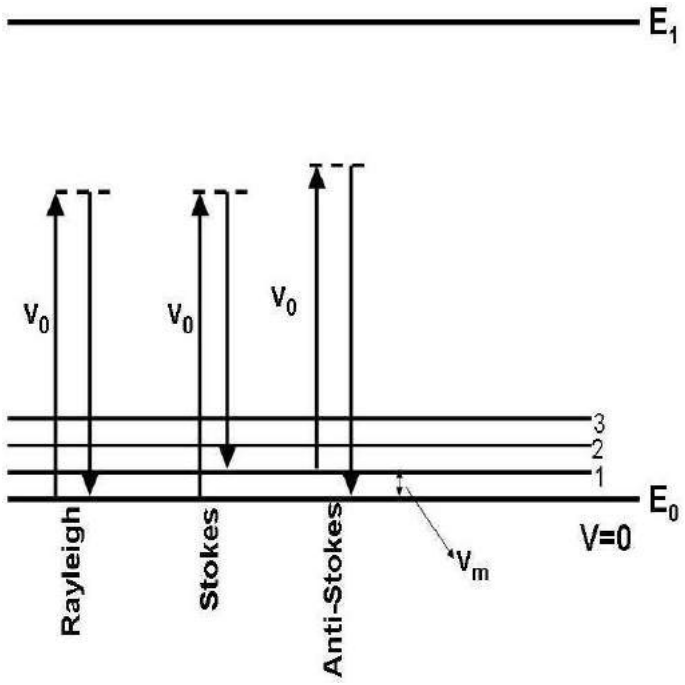

Figure 2.2.2: Energy levels in Rayleigh and Raman scattering.

The figure 2.2.2 shows the Raman scattering in a simple two energy level scheme. E_0 is the ground state, E_1 is the first excited electronic state. The first vibrational states of

the ground state and some virtual states (doted lines) are also shown.

In the Rayleigh scattering the molecule is initially at the ground state, after the absorption a photon of frequency ν_0 it goes to a virtual state with energy $h\nu_0$. From this virtual state the molecule decays to the ground state, emitting a photon of the same frequency of the absorbed one, ν_0.

In Stokes Raman scattering a molecule in the ground state absorbs a photon and goes to a virtual state with energy $h\nu_0$. By emitting a photon with frequency $\nu_0 - \nu_m$, lower than the frequency of the absorbed photon, the molecule decays to a vibrational level of the ground state.

The anti-Stokes Raman scattering happens when a molecule is in a vibrational level of the ground state with energy $h\nu_m$ and by absorbing a photon of frequency ν_0 it goes to a virtual state with energy $h(\nu_0 + \nu_m)$. From this virtual state the molecule decays to the ground state emitting a photon with frequency $\nu_0 + \nu_m$, higher than absorbed one.

From the Maxwell-Boltzman distribution it is known that the population of the ground state $v = 0$ is bigger than the population of the first vibrational state $v = 1$, so the Stokes lines are easier to detect then the anti-Stokes.

2.3 UV-Vis Absorption Spectroscopy

In chemistry is common to make use of colorimetric technique to recognize some species and to determine if reactions are taking place, this is done primarily by the naked eye, but if we use more sophisticated light detectors it is possible to analyze in more detail the interactions of light with these compounds. In general, if a light bean incides in a semitransparent body, part of it will be transmitted and part will be absorbed and part will be scattered. Figure 2.3.3 shows a light bean before and after it goes through a solution of thickness **L** and a concentration **C** of absorbent chemical species (i.e. atoms, molecules, particles). As a consequence of the interaction between the photons and the absorbent species the intensity of the beam is attenuated. The transmittance **T** of the

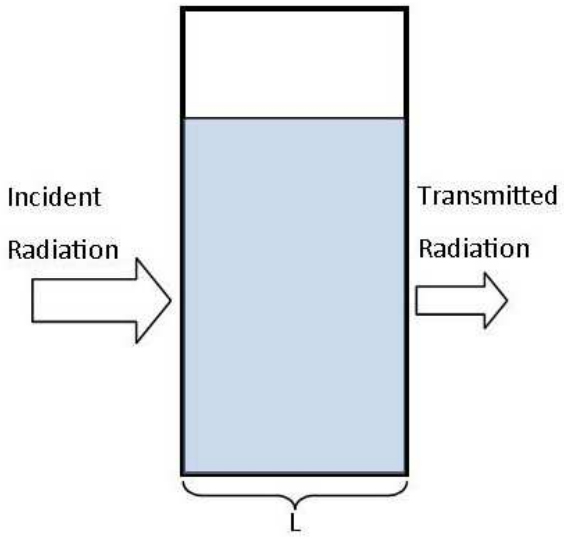

Figure 2.3.3: A light beam incides perpendicularly over a semitransparent material with thickness **L**. The intensity of the transmitted light is lower than the incident light due to the optical absorption and scattering.

solution is defined as the fraction of the incident light transmitted through the solution:

$$T = \frac{I}{I_0} \tag{2.10}$$

and the extinction **A**, the fraction of incident light absorbed by the solution is expressed by the equation:

$$A = -LogT = Log\frac{I_0}{I} = \epsilon CL \tag{2.11}$$

where ϵ is known as the molar absorptivity or extinction coefficient, and this is dependent of both the wavelength of the incident light and the absorbent chemical specie. The later equation is known as the Beer-Lambert law and can be used to determine the concentration of a given solution. If the absorbance is plotted as a function of the wavelength the obtained curve is know as the absorption spectrum. Usually what we measure in the laboratory is the extinction spectrum, this is the absorption plus the scattering; the scattering of light can be thought of as the deflection of a ray from a straight path by irregularities in the propagation medium, particles, or in the interface between two

media (Fig. 2.3.4).

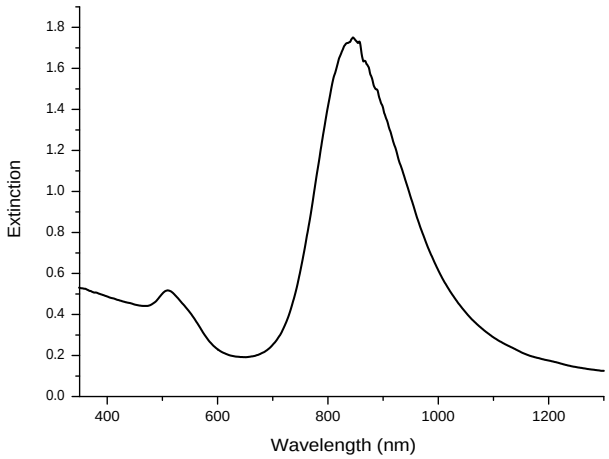

Figure 2.3.4: Extinction spectrum of a gold nanorods colloidal sample.

The interaction of light and small metallic nanoparticles has been object of study for several decades [2, 68]. If the response of these colloids is plotted as a function of the frequency of the incident electromagnetic (EM) field it will be noted that for determined frequencies the extinction coefficient (absorption plus scattering) will present resonant bands known as localized surface-plasmon resonances (LSPR). Surface plasmons are collective excitations of the electrons at the interface between a conductor and an insulator, which are described by evanescent electromagnetic waves that are not necessarily located at the interface [5]. The optical properties of NPs depend on their size, shape, environment, and chemical composition among others parameters.

When noble metals, like gold and silver, are taken to nanometric size these plasmonic resonances are in the visible range of the EM spectrum; if a colloidal solution of these NPs is illuminated with white light, the transmittance of the wavelengths corresponding to these resonances will be diminished, giving us the characteristic extinction spectrum.

One of the interesting features of the NPs colloids is the dependence between the morphology of the particles and their correspondent spectrum. Gold spherical particles

will present only one resonant band; for example, for a gold nanoparticle of 20nm diameter the plasmon band is located around 520nm [3]. On the other hand, a gold nanorod with a diameter around 15-20nm will have a resonant band located around 520nm, and a second plasmon band located from 600 and up to 1200nm, depending in its length [23]. In the same manner particles with anisotropic morphologies (cubes, decahedra , stars, etc.) will present a different spectrum than spherical, this is why these morphologies have been synthesized, so the spectral characteristics can be 'tuned' [5]. The UV-Vis spectroscopy can provide an approximate idea of size and morphology of the metallic colloids [17].

2.4 Techniques

The particle size and morphology were evaluated using transmission electron microscopy (TEM; JEOL, JEM 1230) with an accelerating voltage of 100 kV, Philips, Morgagni 268. Samples used for TEM analysis were prepared by dropping silver nanoparticle colloids onto Formvar/carbon 200-mesh copper grids (Ted Pella Inc.), and allowing them to dry in air at room temperature. Statistical analysis was performed on the TEM images to assess the size of the particles. Twelve images were acquired for each sample in different areas of the grid.

Raman spectra were acquired using a Renishaw InVia microscope Raman spectrometer with an excitation line provided by a diode laser at 785nm. A 5μl drop was placed into a commercial aluminum foil and it was let dry at room temperature.

UV-Vis extinction spectra were recorded using a miniature Stellarnet spectrometer EPP2000 in the wavelength range from 320 to 850nm.

CHAPTER 3

Photochemical Synthesis of Silver Decahedral NPs

Over the past two decades, researchers around the world have been focusing on the design of new and more efficient protocols for the production of metallic nanoparticles and have achieved an incredible variety of sizes and morphologies. The thermal methods are the most straightforward in producing NPs; however, high temperatures and strong reducing agents are required, producing a broad size distribution of NPs. Among the methods used to synthesize NPs, the photochemical synthesis has proven to be a very reliable method to produce diverse morphologies of Ag NPs and narrow size distributions.

This chapter presents the most remarkable results obtained in the photochemical synthesis of silver NPs, an exhaustive study on the photochemical synthesis of silver decahedral NPs is shown; power radiation, different reagents and temperature were analyzed as parameters and the optimal conditions for the photochemical synthesis of decahedral NPs were obtained.

3.1 Methods

For the chemical synthesis of silver spherical nanoparticles, precursor solution, silver nitrate (50mM), sodium citrate tribasic trihydrate (50mM), sodium borohydride (100mM), PVP (5%WV), 50mM Triton X-100, L-arginine (5mM), L-histidine (5mM) and L-lysine (5mM) stock solutions were freshly prepared by dissolving each reagent in Milli-Q water.

3.1.1 Power radiation

It is known that by increasing the irradiance (light intensity per unit of area) on the precursor solution, it is possible to shorten the time required for the synthesis to reach completion and to control the size of the NPs. However, few reports have shown a systematic photochemical synthesis at different irradiances [28, 29, 33, 46, 47]. We first explored the kinetics of the photochemical synthesis of Ag decahedrons under different irradiances using blue light. To evaluate the role of the irradiance, a set of precursor solutions were prepared with and without the L-lysine amino acid. Each solution contained 4ml of deionized water in a small, 20ml beaker to which 0.285ml of sodium citrate (50mM), 0.009ml of PVP (5%WV), 0.114ml of $AgNO_3$ (50mM) and 0.045ml of $NaBH_4$ (100mM) were added sequentially under continuous magnetic stirring to obtain a homogeneous precursor solution. Precursor solutions were transferred to 4ml plastic cuvettes. For the amino acid samples, 0.030ml of L-lysine (5mM) was added prior to transferring the solution to the cuvette. All samples were kept at rest for 30min before illumination under blue LED radiation at 80, 50 and 15mW/cm^2 during the photochemical synthesis.

3.1.2 Aminoacids

In a previous report, Pietrobon and Kitaev[33] used L-arginine to control the size and morphology of Ag decahedral NPs, which also had the advantage of being a photochemical promoter. L-Arginine is one of the essential amino acids with an electrically positive charged side chain similar to that of L-histidine and L-lysine. We hypothesize

that if L-arginine is useful in controlling the formation of decahedrons, then L-lysine and L-histidine may also be useful due to their similar biochemical characteristics. We were interested in exploring the kinetics of photochemical syntheses in the presence of different amino acids. Different precursor solutions were prepared with different volumes/concentrations of amino acids in the following manner: 0.285ml of sodium citrate (50mM), 0.009ml of PVP (5%WV), 0.114ml of $AgNO_3$ (50mM) and 0.045ml of $NaBH_4$ (100mM) were taken from the stock solutions and added sequentially to 4ml of deionized water in a beaker under continuous stirring as a precursor solution. A set of plastic cuvettes was then filled with 0.010, 0.030, 0.050 and 0.070ml of L-arginine (5mM), and the precursor solution was transferred to each cuvette (4ml). The same procedure was followed for L-lysine and L-histidine. Samples were kept at rest for 30min prior to irradiation.

3.1.3 Surfactants

We were interested in determining whether other surfactants aside from PVP permit the formation of silver nano-decahedrons by means of the photochemical synthesis using blue light. For this reason, we prepared different precursor solutions using CTAB, CTAC and Triton X-100 as stabilizers instead of PVP and followed the same procedure as described above. Surfactants CTAB and CTAC do not permit the formation of new species or changes in the size of Ag NPs under blue irradiation, while Triton X-100 exhibits similar kinetics of those produced with PVP. For this reason, we prepared several samples of 0.285ml sodium citrate (50mM), xml of 0.05M Triton X-100 (where x = 0.100, 0.080, 0.060 and 0.020ml), 0.114ml of $AgNO_3$ (50mM), 0.045ml of $NaBH_4$ (100mM) and 0.030ml of L-lysine (5mM) in 4ml of milli-Q water in a beaker under continuous stirring to obtain homogeneous precursor solutions. All samples were kept at rest for 30min prior to irradiation.

3.1.4 Temperature

Many reports have proposed the use of temperature for controlling the size and morphology of Ag NPs in one- or two-step processes, and nanocubes, nanoplates and nanoprisms are some of the most common morphologies obtained [14, 25, 69–72]. Only a small amount of work has been performed using temperature and irradiation simultaneously to control the size and morphology of silver decahedrons. In this work, we performed a photochemical synthesis of silver nanoparticles at different temperatures to determine the effect of temperature on the resulting nanoparticle characteristics. In this experiment, sets of eight samples were prepared, four with PVP and four with Triton X-100. The samples with PVP were prepared in 4ml of deionized water in a 20ml beaker to which 0.285ml of sodium citrate (50mM), 0.009ml of PVP (5%WV), 0.114ml of $AgNO_3$ (50mM) and 0.045ml of $NaBH_4$ (100mM) were added sequentially, and this solution was added to 0.03ml of L -lysine (5mM) in plastic cuvettes. The samples prepared with Triton X-100 were prepared in a similar manner but with 0.06ml of Triton X-100 (0.05M) instead of 0.009ml of PVP.

3.2 Results

Photochemical processing seems to offer good size and morphology control through the selection of appropriate surfactants, photocatalytic molecules and wavelengths of light. While many authors have reported studies utilizing the photochemical method, several questions remain regarding the role of some important parameters that control the photochemical synthesis. In this part, we systematically studied the photochemical synthesis of silver nanoparticles by monitoring the concentration of amino acids and surfactants, the irradiance and the solution temperature during the synthesis. Details on the preparation of these sample can be found in section 3.1.

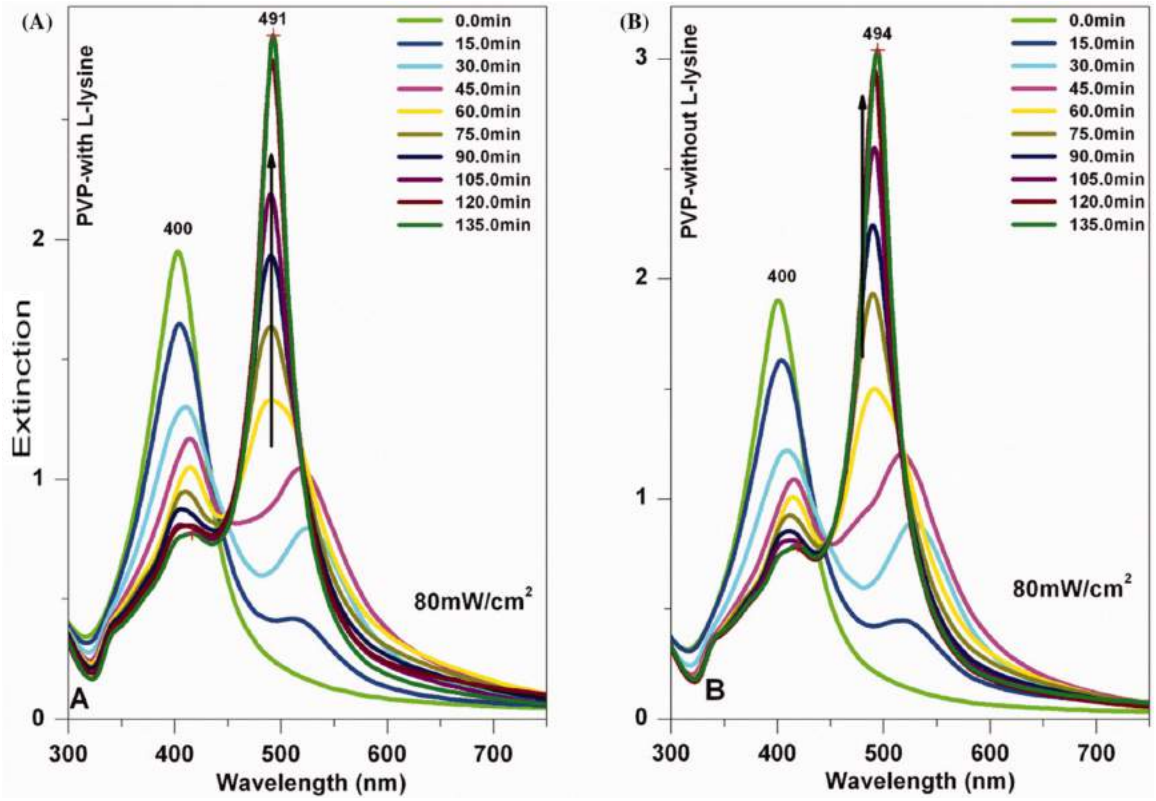

Figure 3.2.1: Spectral evolution of silver precursor solutions irradiated with blue light (LEDs) with an irradiance of 80mW/cm^2. The spectra were measured every 15min for solutions prepared (A) with L-lysine and (B) without L-lysine.

3.2.1 Power Radiation

Silver decahedron NPs were prepared by the photochemical transformation of a precursor solution using commercial blue LEDs under several irradiances. Figure 3.2.1 shows the mean UV-Vis extinction spectra taken during the photochemical synthesis for two samples, one prepared with L-lysine and the other without the amino acid; both precursor solutions were irradiated at 80mW/cm^2. We observed that both samples exhibited similar kinetics.

The plasmon band of the precursor solutions was located at 400nm, the extinction

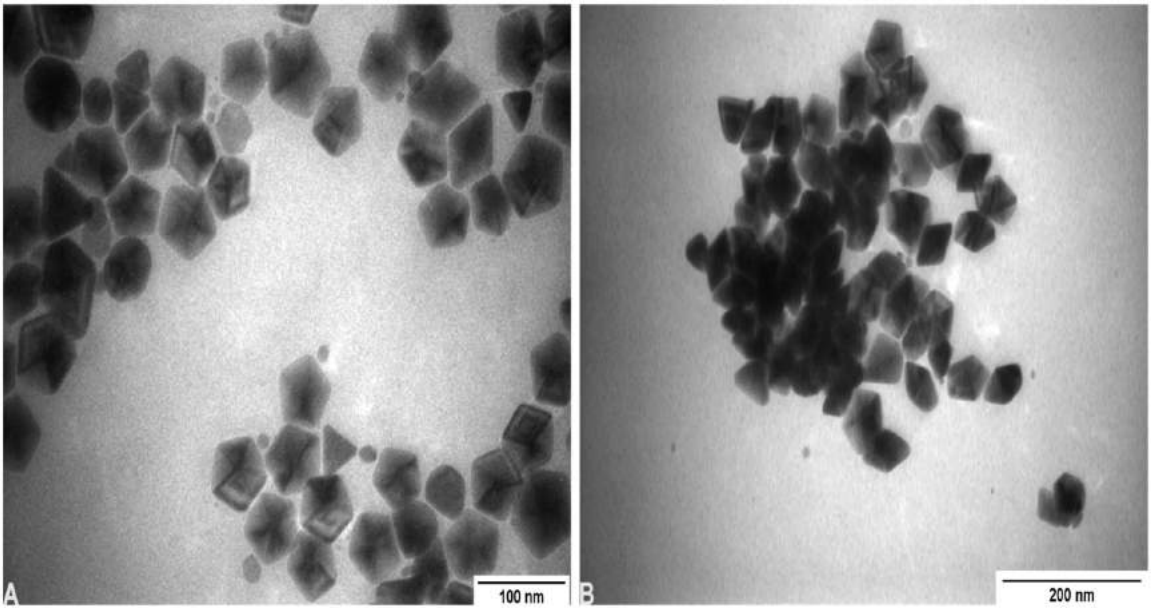

Figure 3.2.2: TEM images of silver nanoparticles produced by photochemical synthesis (A) with L-lysine (obtaining a mean size of 57 nm and 63% decahedral nanoparticles) and (B) without L-lysine (obtaining a mean size of 57 nm and 32% decahedral nanoparticles) and with bipyramidal nanoparticles 65nm in length and 42nm in width.

of this peak started to decrease several minutes after irradiation was initiated, and a new peak appeared (corresponding to the in-plane plasmonic mode) and exhibited a bathochromic (red) shift, which tuned the plasmon band at 530nm. A hypsochromic (blue) shift was then observed, which tuned the plasmon band to 491 and 494nm for samples with and without L-lysine, respectively. The extinction we observed at a time of 135min was higher for samples without L-lysine, and its peak was slightly wider; however, the time of the full synthesis was almost the same for both cases. From these results, it seems that L-lysine do not help to improve the synthesis of silver decahedron NPs because the kinetics of the syntheses are very similar. However, the TEM images of these NPs show significant differences. Colloids produced in the presence of L-lysine show an improved monodispersion of the Ag decahedron NPs (62% decahedral NPs),

while the colloids obtained without L-lysine produce NPs with a variety of morphologies, including decahedrons (only 32%), triangles, plates and especially bipyramidal nanoparticles, as shown in Figure 3.2.2. We then prepared new precursor solutions with the same stochiometry, and the samples were irradiated at 50 and 15mW/cm^2 using the same blue LEDs. Figure 3.2.3 shows the kinetics of the photochemical syntheses for the three different irradiations, where the band of maximum extinction for the final product was plotted as a function of irradiation time for each irradiation condition. We observed similar behavior between the samples made with and without amino acids under the same irradiance conditions. It is clear that samples exposed to 80mW/cm^2 require less time for the completion of the synthesis, with almost 120min required to reach at least 2 optical densities, while for similar samples exposed to 50 and 15mW/cm^2, it takes approximately 165 and 270min, respectively. This means that the higher the irradiance, the shorter the time required for the completion of the synthesis and the greater the percentage of silver decahedron nanoparticles formed. The bathochromic shift of the plasmon frequency indicates the initiation of a photochemical process upon blue irradiation, and it does not depend on the presence or absence of the amino acid. The hypsochromic shift indicates the formation of new morphologies followed by the nucleation or aggregation of seed particles. The power radiation only caused small variations in the final location of the plasmon frequency, but was still significant for irradiances of 80 and 50mW/cm^2; the maximum shifts were located at approximately 492nm for amino acid samples (L-lysine) and 494nm for samples without the amino acid, while samples irradiated with 15 mW/cm^2 exhibited a shorter hypsochromic shift at 498nm both with and without the amino acid. The photochemical synthesis was not conducted for irradiances higher than 80mW/cm^2 due to the limitations of our source, but our results suggest that higher radiant flux densities can help shorten the time required for the completion of the photochemical synthesis. Increasing the flux does not, however, guarantee that the morphology produced will consist of decahedrons.

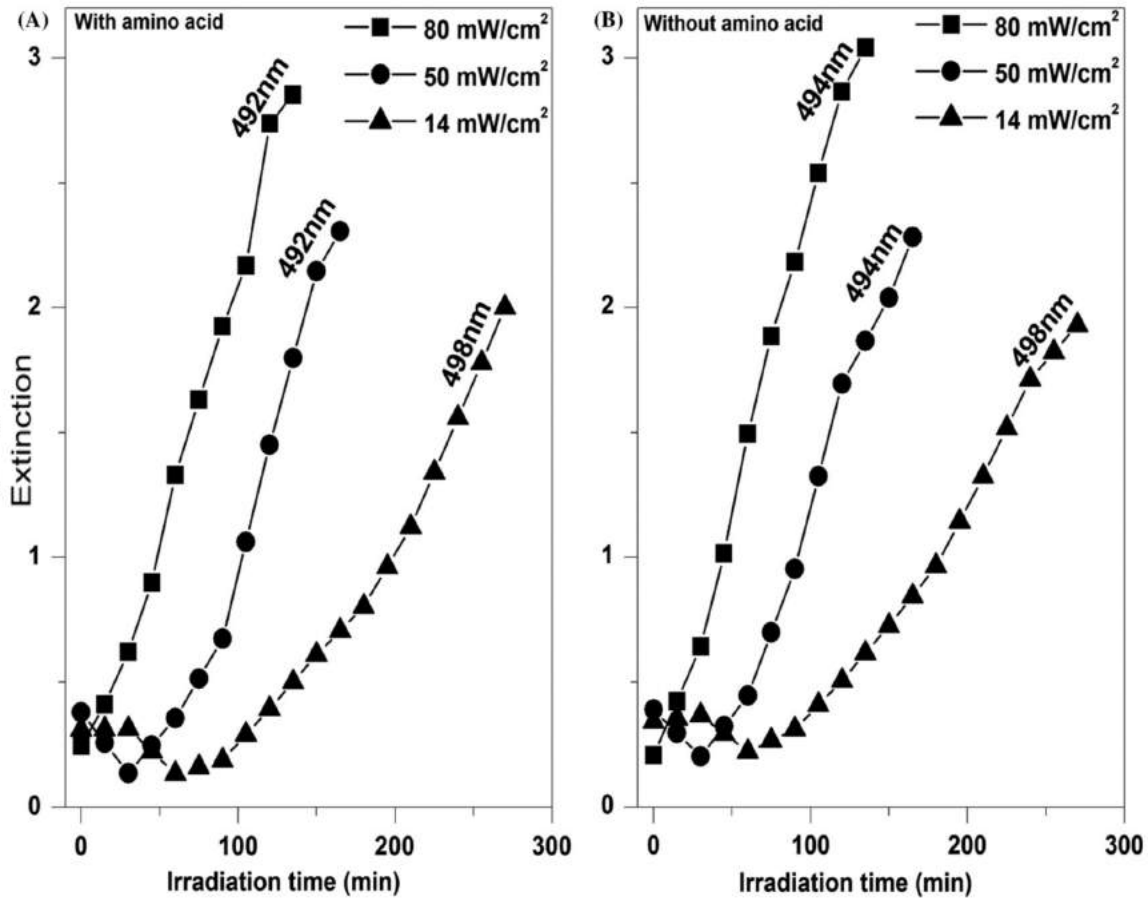

Figure 3.2.3: The kinetics of the precursor solutions followed under different irradiances (80, 50 and 15mW/cm^2) (A) with L-lysine and (B) without L-lysine as represented by the maximum of the in-plane dipole resonance extinction band as a function of the irradiation time.

3.2.2 Amino Acids

To explore the role of the amino acids and their concentrations, we followed the kinetics of the silver precursor solution in the presence of three different amino acids (L-arginine, L-lysine and L-histidine) with positively charged side chains. The samples were prepared as outlined in Section 3.1.2. In accordance with the power radiation experiments, all samples were exposed to blue light (LED) using the maximum irradiance (80mW/cm^2).

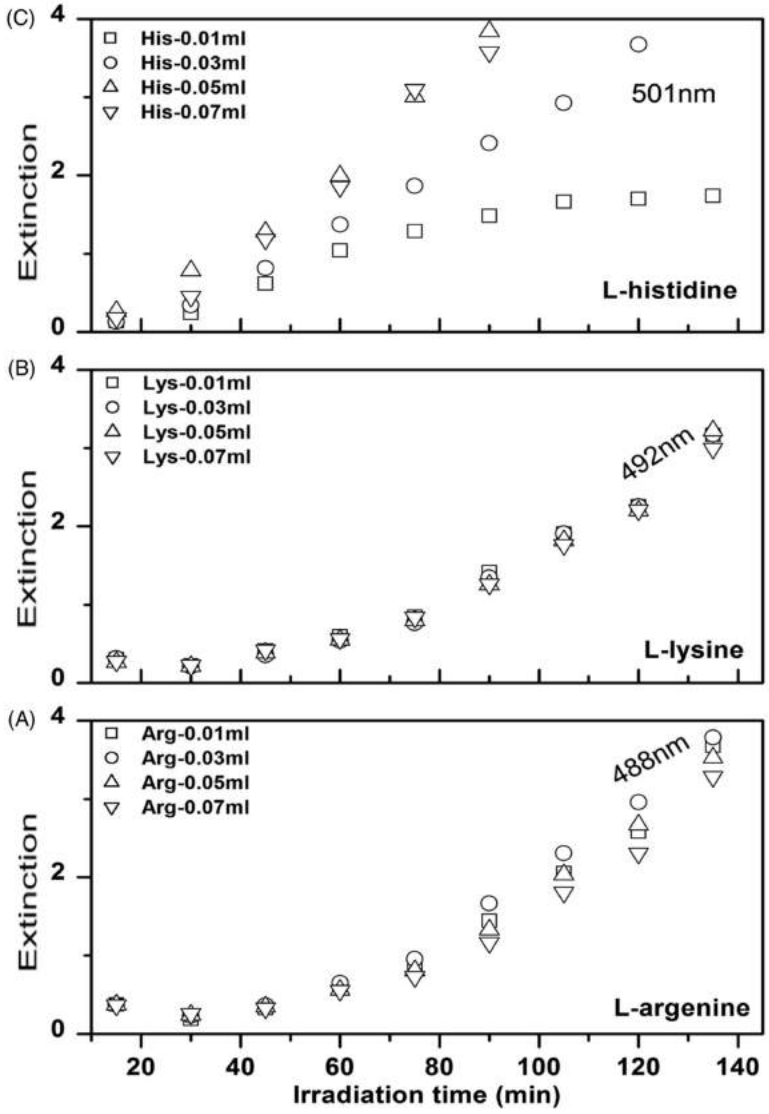

Figure 3.2.4: The maximum of the in-plane dipole resonance extinction band as a function of irradiation time of the precursor solutions with (A) L-arginine, (B) L-lysine and (C) L-histidine, followed by an irradiation of 80mW/cm^2.

The kinetics of the photochemical syntheses were again followed by recording the UV-Vis extinction spectra for every 15min.

Figure 3.2.4 shows the maximum extinction band of the second peak for the final

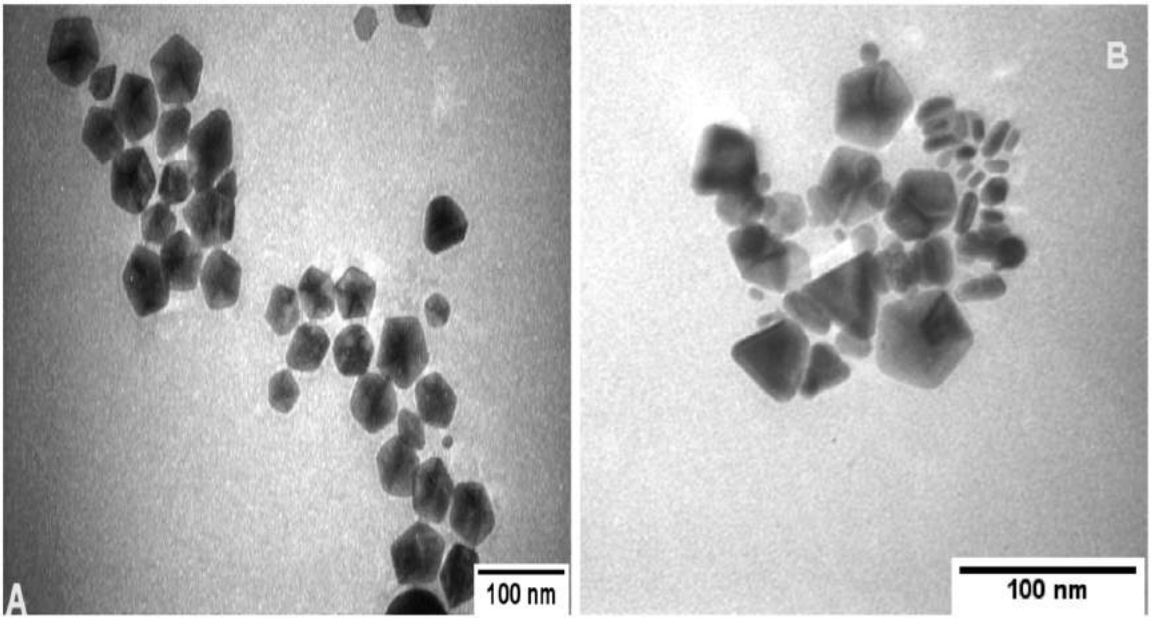

Figure 3.2.5: TEM images of silver nanoparticles produced by the photochemical synthesis with (A) L -arginine (60% decahedral nanoparticles with a mean size of 50nm) and (B) L -histidine (15% decahedral nanoparticles with a mean size of 45nm).

product as a function of irradiation time for the three amino acids (488, 492 and 501nm for L-arginine, L-lysine and L-histidine, respectively). Our results show that precursor solutions prepared with L-arginine and L-lysine exhibit similar kinetics during the photochemical synthesis for different volumes/concentrations (0.01, 0.03, 0.05 and 0.07mL) of the amino acid (Figures 3.2.4A-B). The bathochromic (530nm) and hypsochromic (488nm for L-arginine and 492nm for L-lysine) shifts are very similar for both cases, with only small differences observed in the extinction values. We believe that the existence of similar kinetics during the photochemical synthesis will result in both amino acids, improving the formation of silver decahedrons. It is also evident from the TEM images that there is a high yield of decahedral particles, as shown in Figures 3.2.2A and 3.2.5A (63% and 60% decahedral nanoparticles, respectively). According to the TEM images, the mean size of the decahedral nanoparticles was 50nm when synthesized with

L-arginine and 57nm when synthesized with L-lysine. The kinetics of the synthesis with L-histidine show significant differences, with small variations in concentration causing significant variations in the kinetics of the synthesis (Figure 3.2.4C). Samples prepared with 0.01mL of L-histidine stabilized at approximately 135min and yielded an optical density of 1.38, while samples prepared with 0.07mL of L-histidine reached an optical density greater than 3 and required approximately 90min to finish the synthesis. TEM images reveal that for these samples, a low yield of silver decahedrons (only 15%) was produced, as other morphologies were observed, including triangles and rods (Figure 3.2.5B). The rods had diameters ranging from 6 to 10nm, and the mean length of the rods was between 13 and 23nm. The triangles had a size of 46nm from corner to side. The mean size of the decahedrons from the L-arginine samples was 50nm, and the plasmon peak was located at approximately 491nm, while for the L-histidine decahedrons, the mean size of the nanoparticles was 45nm, and the plasmon band was located at approximately 501nm. From these results, we can conclude that the maximum irradiance from blue LEDs together with L-arginine or L-lysine permits the improvement of the formation of silver decahedrons, at least under the chosen experimental conditions.

3.2.3 Surfactants

We were also interested in exploring other combinations of surfactants for the production of decahedron nanoparticles using the photochemical synthesis. To this end, Triton X-100, CTAB and CTAC were used instead of PVP. Triton X-100 was the only surfactant that showed any photochemical changes among the precursor solutions examined, and thus, new precursor solutions were prepared with varying volumes/concentrations of Triton X-100 (0.10, 0.08, 0.06 and 0.02mL; see Section 3.1.3). All samples were kept at rest for 30min prior to exposure to blue light at 80mW/cm^2. Figure 3.2.6A shows the typical UV-Vis extinction spectra for samples prepared with 0.60mL of Triton X-100. Figure 3.2.6B shows the kinetics of the photochemical synthesis for the four samples. The time of the synthesis was approximately 135min. Samples with lower volumes/concentrations

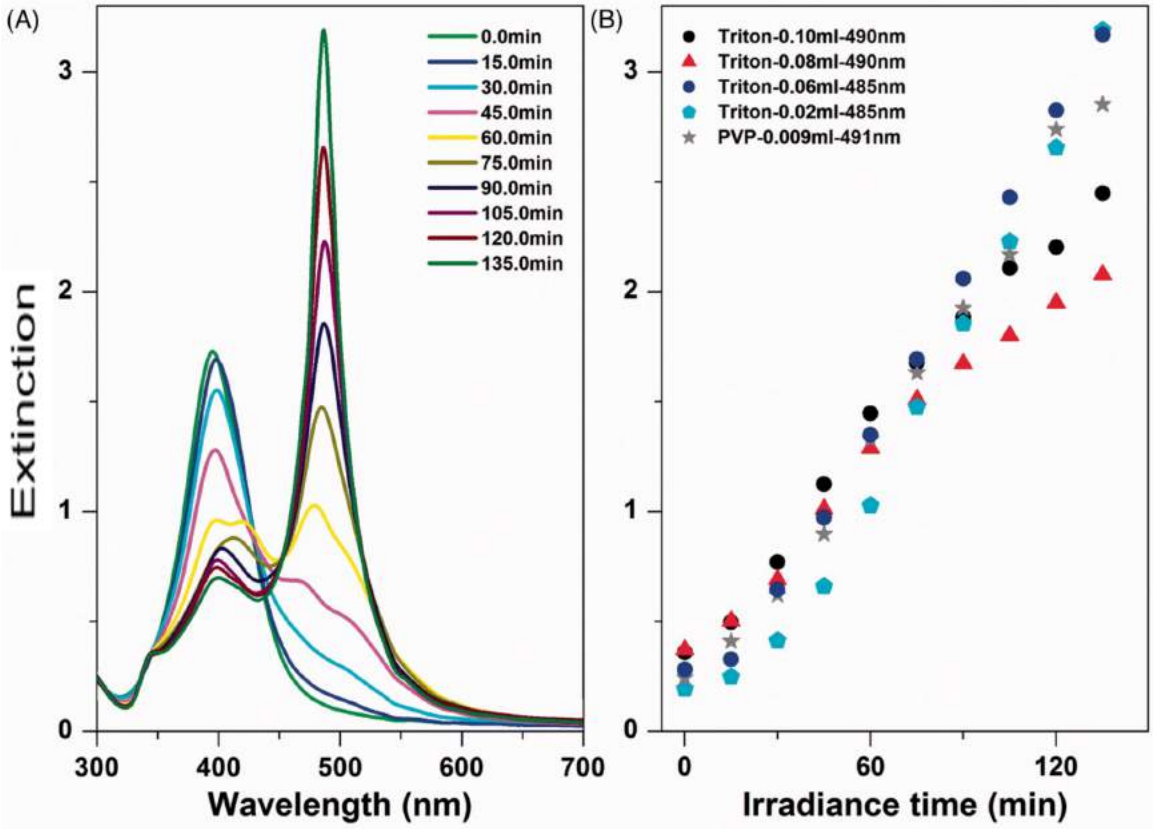

Figure 3.2.6: Spectral evolution of the silver precursor solution prepared with 0.06mL of Triton X-100 and irradiated with blue light (LEDs) at 80mW/cm^2 with spectra taken every 15min(A). The maximum of the in-plane dipole resonance extinction band as a function of the irradiation time, representing the kinetics of the photochemical synthesis for different volume concentrations of Triton X-100 (B).

of Triton X-100 reached optical densities of approximately 3, while those with higher volumes of Triton X-100 reached optical densities of approximately 2. Comparing the UV-Vis spectra of Figure 3.2.1, we can see that the second peak, which provides information regarding the production of decahedrons, shows a bathochromic shift, tuning the plasmon band to 530nm, after which a hypsochromic shift occurs and the colloids then stabilize at approximately 491nm. Only the hypsochromic shift of the second peak is

present for Triton X-100 samples, as shown in Figure 3.2.6A. The hypsochromic shift of the second peak of the Triton X-100 samples stabilizes at approximately 485nm for the first two samples and at 490nm for the last two samples. From a kinetics standpoint (Figure 3.2.6B), we can assume that new silver nanoparticles are forming, but it seems that the morphology is not consistent with decahedrons. TEM images taken for these colloids are in agreement with this kinetics argument, and silver nanoparticles were produced with a mean size of 41nm, but they resemble more closely to spherical particles than decahedrons (Figure 3.2.8C). This shows that the photochemical synthesis occurs with Triton X-100, but it does not produce silver decahedrons at this temperature.

3.2.4 Temperature

Reports have shown that temperature helps to improve the chemical synthesis of silver and gold nanoparticles, and triangles and plates can be produced at temperatures ranging from 50^{o}C to 100^{o}C [14, 27, 73–76], but the use of temperature and light irradiation simultaneously to control the synthesis of silver nanoparticles has not been reported. In this section, we show the results obtained from the photochemical synthesis of silver nanoparticles under different temperature conditions. The precursor solutions were transferred to 4mL quartz cuvettes, and all of the samples were at rest for 30min before heating. They were allowed to sit on a hot plate for 30min to reach thermal equilibrium at 60, 52, 46 and 40^{o}C prior to irradiation of the samples. The extinction spectra were taken at 15min intervals during irradiation. The evaporation of water was compensated through the addition of water at the same temperature as the colloid solution to maintain the total volume during the synthesis. The kinetic behavior of the synthesis is shown in Figure 3.2.7; the synthesis was stopped when the colloid showed minimal variations in its extinction, as this implies that the temperature and radiation do not result in the formation of new nanoparticles at the same rate as in the initial stages. Samples set at 60^{o}C and prepared with PVP reached optical densities of 2, while samples prepared with Triton X-100 reached optical densities of 0.4. At lower temperatures, the colloids

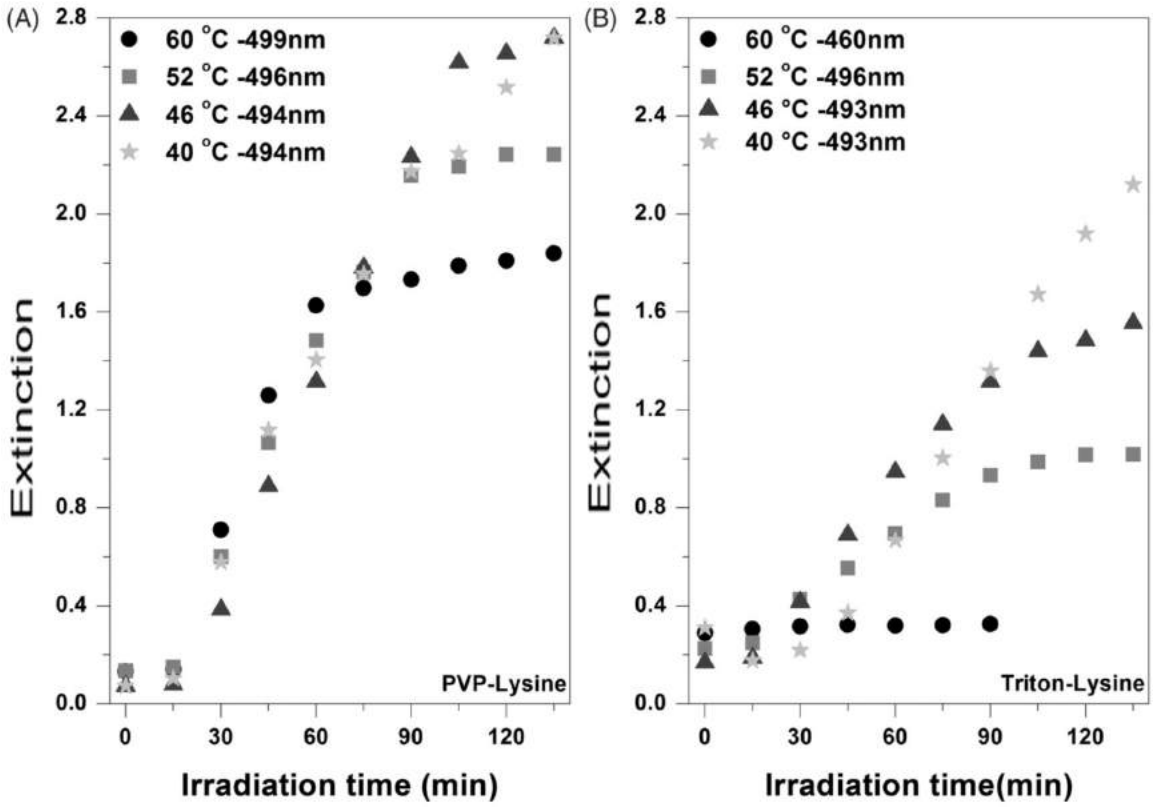

Figure 3.2.7: The maximum of the in-plane dipole resonance extinction band of silver precursor solutions irradiated at 80mW/cm^{2}as a function of the irradiation time (followed at 60, 52, 46 and 40^{o}C) with (A) PVP and (B) Triton X-100 as surfactants.

stabilized over longer periods of time but yielded high optical density values, implying that decahedrons or other particle types are being produced. After reviewing the TEM images in Figure 3.2.8, we observed that colloids produced with PVP at temperatures of 40^{o}C and 46^{o}C seem to have improved monodispersion of silver decahedrons (63% and 75% decahedral particles, respectively). The mean sizes of these samples were 58 and 55nm, respectively. We can see from the TEM images that other morphologies are almost absent. Similar results were observed for the case of Triton X-100, where decahedrons were not produced at room temperature. At 40^{o}C and 46^{o}C, however, we were able to produce silver decahedron nanoparticles (56% decahedral nanoparticles), triangles and

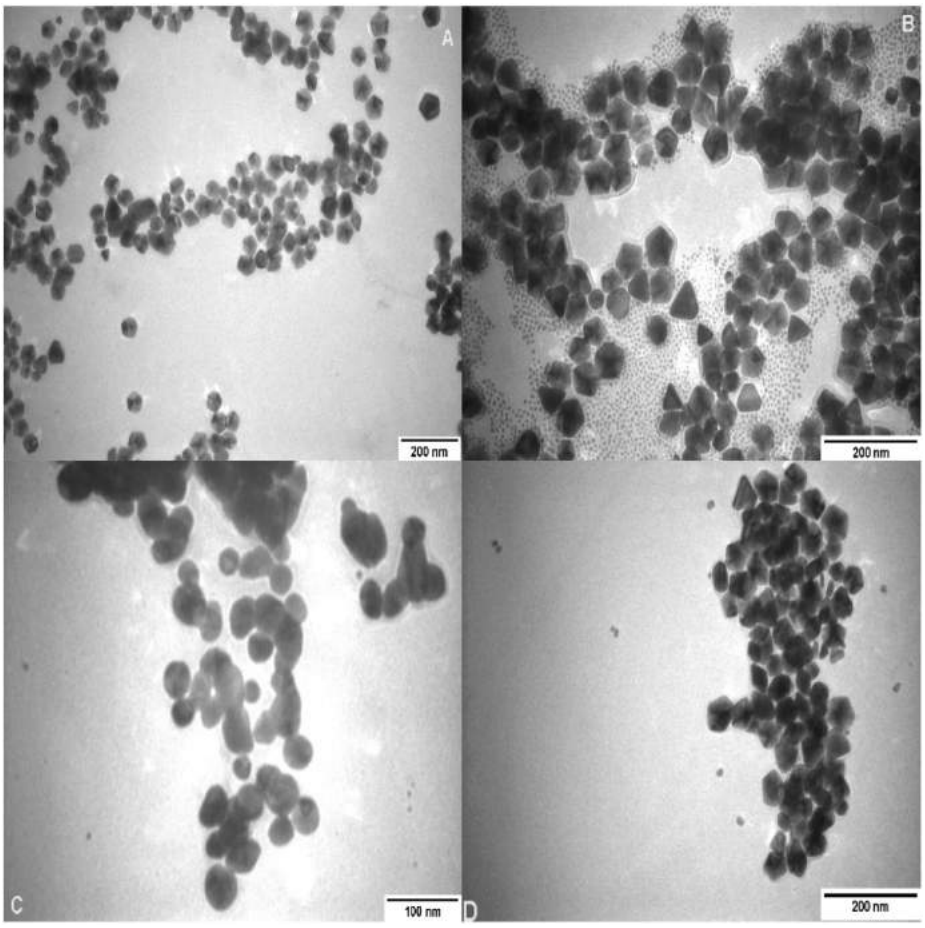

Figure 3.2.8: TEM images of silver nanoparticles produced by photochemical syntheses (A) with PVP and L -lysine at 40^{o}C (63% decahedral nanoparticles, mean size of 58nm), (B) with PVP and L -lysine at 46^{o}C (75% decahedral nanoparticles, mean size of 55nm), (C) with Triton X-100 and L -lysine at room temperature (0% decahedral nanoparticles) and ID) with Triton X-100 and L -lysine at 46^{o}C (56% decahedral nanoparticles, mean size of 54nm).

bypiramids. For the case of Triton X-100 at 60^{o}C, the synthesis did not proceed as well as at the other elevated temperatures examined, decahedrons were again absent, and a variety of morphologies was observed. The use of PVP and the amino acids always resulted in the production of decahedron nanoparticles with different yields, but for the case of Triton X-100, we were able to obtain decahedrons only by increasing the temperature of

the photochemical synthesis between 40 and 46^{o}C.

3.3 Conclusions

In section 3.2, the synthesis of stable silver decahedron nanoparticles produced under blue light irradiation (LEDs) of silver precursor solutions is reported. In this part, we systematically studied the photochemical synthesis of silver nanoparticles by monitoring the concentration of amino acids and surfactants, the irradiance and the solution temperature. To improve the formation of the decahedrons under blue light irradiation, we used three amino acids with electrically charged side chains (L-arginine, L-lysine and L-histidine). The results show that L-arginine and L-lysine are best suited for improving the yield of decahedrons. This is primarily because small variations in the concentration of L-histidine yielded large variations in the kinetics of the synthesis and also because the decahedron yield was lower for L-histidine (15%) than for L-lysine (63%) and L-arginine (60%). We followed the kinetics of the photochemical synthesis under different irradiations of 80, 50 and 15mW/cm^2. The maximum irradiation of 80mW/cm^2 resulted in a two-fold reduction in the time required for the synthesis to come to completion with respect to the lower irradiances. One of the most interesting results was obtained when preparing the precursor solution with Triton X-100 instead of PVP as the surfactant. The photochemical synthesis was performed at different temperatures under these conditions, and we noticed the improvement of decahedral nanoparticle formation at temperatures between 40^{o}C and 50^{o}C for both cases. When PVP was used as the surfactant and the photochemical synthesis was performed at either 40^{o}C or 46^{o}C, we obtained 63% and 75% decahedral nanoparticle formation, respectively. When performing this experiment with Triton X-100, decahedral nanoparticle formation was not observed at room temperature but was found to result in 56% formation at 46^{o}C.

With this it has been demonstrated that the photochemical synthesis of silver decahedral NPs is a multifactorial process in which every variable needs to be optimized to

increase the yield of decahedral NPs.

CHAPTER 4

Photochemical Transformation of Ag NPs by Combining Blue and Green Irradiation

In Chapter 3, it was shown the formation of silver decahedral nanoparticles by using a single light source. Now in the present Chapter, it will be shown that it is possible to tune the optical properties of the silver NPs in a wider range and to obtain a variety of morphologies by combining two light sources at different times during the synthesis.

4.1 Methods

First, silver nitrate (50mM), sodium citrate tribasic trihydrate (50mM), sodium borohydride (100mM), protoporphyrin IX (88μM), and PVP (5% WV) stock solutions were freshly prepared by dissolving each reagent in Milli-Q water. For the synthesis of the precursor solution, 36ml of Milli-Q water were placed in a beaker under vigorous magnetic stirring; then 2571μl of sodium citrate solution, 810μl of PVP solution, 103μl of silver nitrate solution, 270μl of PPIX solution, and 411μl of sodium borohydride solution were

added sequentially. The addition of sodium borohydride changed the precursor solution from a clear to a yellowish one, indicating the presence of small nanoparticles (diameter 3±1nm). The precursor solution was kept in the dark for at least 2 hours before light irradiation. Commercial blue (λ_0=465nm, 180mW/cm^2) and green (λ_0=520nm, 50mW/cm^2) LEDs were used as light sources for the photochemical transformation of the nanoparticles.

A set of 11 samples was prepared by transferring 2ml of the precursor solution to disposable plastic cuvettes (0.4cm of path length). Samples A1 and A2 were, respectively, irradiated by blue and green LEDs. Samples A3 to A11 were initially irradiated by blue LEDs for given times of 2, 3, 4, 5, 10, 15, 30, 45, and 60min; after that, green radiation was used until 150min had elapsed. By monitoring the UV-Vis optical extinction spectrum every 15min during the entire photochemical synthesis process, the kinetic growth of the NPs was followed. All the experiments were carried out three times to check reproducibility of the synthesis.

Additionally, some experiments were conducted by first irradiating the silver precursor solutions with green light for different specific times (15 and 30min); then, blue radiation was used until no more changes in the extinction spectrum were observed. In this case, no significant changes were noticed: all the samples showed the same plasmon band at the end of the synthesis

4.2 Results

Silver nanoparticles of different sizes and morphologies were prepared through a light assisted transformation method, by exposing the silver precursor solution to blue and green radiation, and by using protoporphyrin IX (PPIX) as a photopromoter. At the beginning of the photochemical synthesis, the precursor solution presented the out-of-plane dipole surface plasmon resonance (OPD-SPR) band located at 400nm, indicating the presence of small silver NPs (Fig. 4.2.1A), such as it has previously been reported

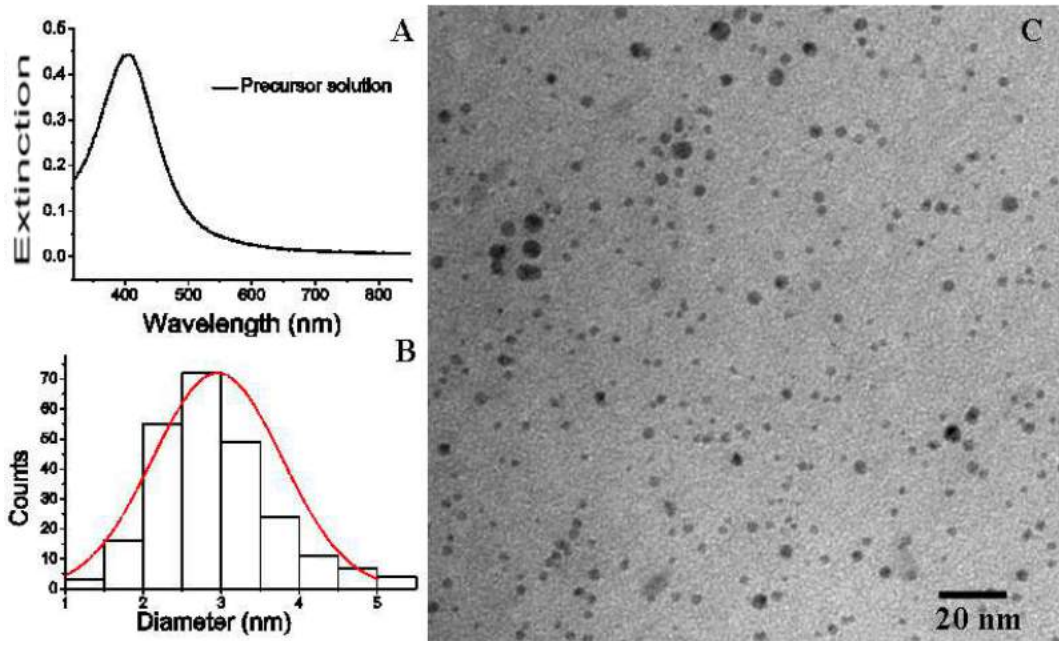

Figure 4.2.1: UV-Vis extinction spectrum (A), size distribution (B), and transmission electron microscopy image (C) of the precursor solution of silver nanoparticles.

[28, 29, 33, 39]. The TEM image shows that the precursor solution consists mainly of spherical nanoparticles with a mean diameter of 3±1nm (Fig. 4.2.1B, C).

4.2.1 Light Assisted Transformation Under Blue Irradiation

Sample A1, with an unique plasmon band at 400nm, was irradiated only by blue light and monitored by recording the UV-Vis spectra; after 5min of irradiation, a new band appeared at 500nm, see Fig. 4.2.2A. This band is assigned to the in-plane-dipole surface plasmon resonance (IPD-SPR), followed by a bathochromic shift (red shift) with a maximum at 520nm and an extinction value of 0.85 after 15min of irradiation. The band at 400nm decreased drastically to get an extinction value of 0.21. The decrease of the OPD-SPR band (400nm) means that seeds were diminishing significantly, but were still observed at a lower concentration. On the other hand, the TEM image (see Fig.

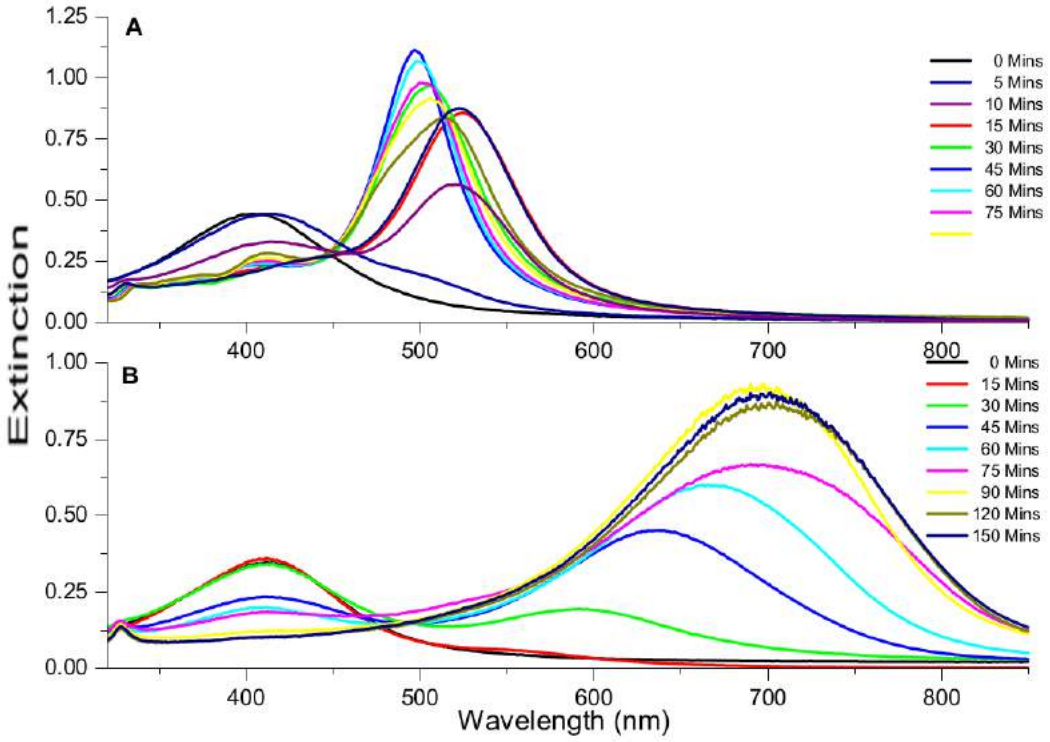

Figure 4.2.2: UV-Vis extinction spectra of samples A1 and A2 (panels A and B, respectively) at different stages during the photochemical transformation.

4.2.3) shows that twin NPs with a mean diameter 18±6nm of were produced. Thereafter, the colloidal solution displayed a hypsochromic shift (blue shift) up to 496nm, and the extinction value increased to 1.10 at 45min of blue irradiation. A carefully revision of the TEM images revealed that twin nanoparticles increased in number (with a mean size of 28±9nm); additionally, spherical and decahedral nanoparticles appeared, both with mean sizes of 12±4nm and 39±8nm, respectively. A new bathochromic shift happened after some minutes of stabilization, and the band at 496nm shifted to 511nm, with an extinction value of 0.8. Furthermore, the band at 400nm increased its extinction from 0.21 to 0.29, meaning that the oxidative process occurred, and particles of smaller size

were produced, which permitted that decahedron nanoparticles grew to get a final mean size of 78±13nm. The TEM image corresponding to the end of the synthesis under blue irradiation shows that decahedral is the dominant morphology (Fig. 4.2.4).

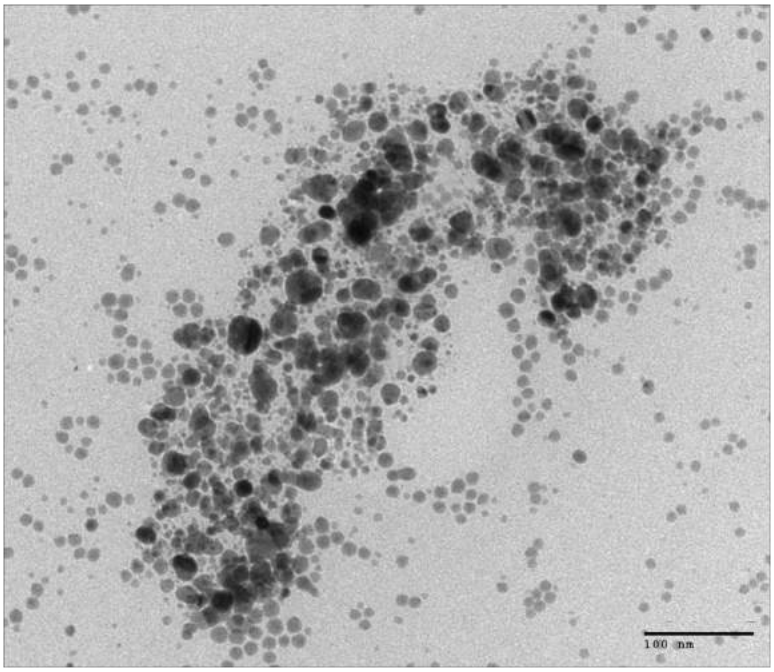

Figure 4.2.3: TEM image of sample A1 at 15 minutes of blue light irradiation. Disk and twin nanoparticles with a mean size of 18±6nm are the dominant morphologies in this stage of the synthesis.

4.2.2 Light Assisted Transformation Under Green Irradiation

The precursor solution irradiated with green light, sample A2, was monitored by recording the UV-Vis spectra. The spectra showed significant changes in the extinction and in the shift of the plasmon band from sample to sample during all the kinetic growth process; we noticed poor reproducibility of the photochemical synthesis, here we report the best results obtained. The general behavior of the kinetic growth can be described in the following way: a new plasmon band began to appear at 560nm during the first 15min of irradiation (Fig. 4.2.2B); this band is assigned to the IPD-SPR band. At 30min of

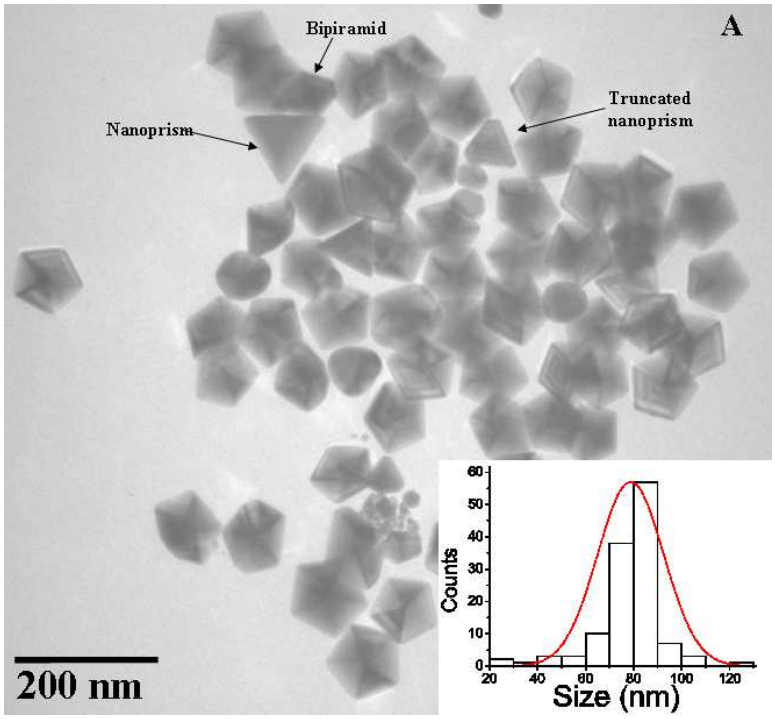

Figure 4.2.4: TEM image (A) and size distribution (B) of sample A1, synthesized under blue radiation.

irradiation, the IPD-SPR band exhibited a bathochromic shift up to 590nm, and the extinction value increased from 0.02 to 0.19, indicating the growth of non spherical NPs. At this time, the TEM images showed a variety of morphologies: twin (size 37±22nm), flat (<20nm) and seed particles (see Fig. 4.2.5). Furthermore, these images showed several stacked flat NPs, with an average thickness of 7±2nm.

After 30min, the growth rate changed, and the transformation occurred faster, such as the UV-Vis spectra display. In fact, at 45min of synthesis, the IPD-SPR band shifted to 633nm, and the extinction increased to 0.44. On the other hand, the OPD-SPR band assigned to the precursor solution decreased its extinction value from 0.36 to 0.23, indicating that the number of seeds had diminished significantly. The TEM images showed a great variety of nanoparticles: mostly flat rounded (size 21±8nm), along with some flat triangles and twin NPs, while the stacked NPs showed an average thickness of

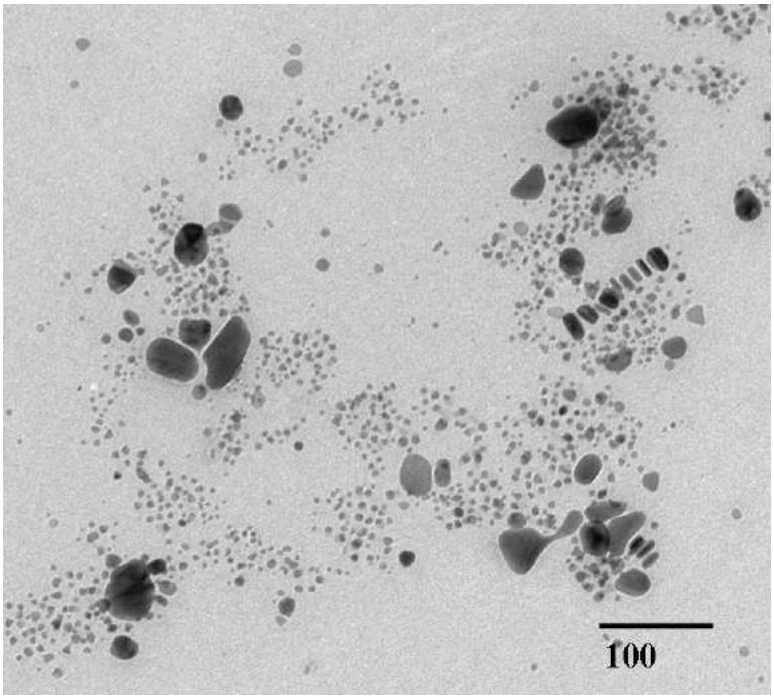

Figure 4.2.5: TEM image of sample A2 at 30 minutes of green light irradiation. Twin nanoparticles with a mean size of 37±22nm were the dominant morphologies in this stage of the synthesis. Also flat (<20nm) and seed nanoparticles are present.

7±2nm, see Fig. 4.2.6.

As the photochemical process went on, the UV-Vis spectra show that the bathochromic shift of the IPD-SPR band continued, shifting up to 694nm at 75min of synthesis. The extinction in the original 400nm band decreased to 0.18 (Fig. 4.2.2B), and the band at 330nm, associated to the interband transitions, is now identified [5]. It seems that the particles were still being transformed in size and morphology; seed and twin particles had been significantly diminished, and flat rounded was the dominant morphology observed. TEM images show several stacked nanoparticles, both tilted and flat, with a 23±6nm mean size and 6±2nm mean thickness (Fig. 4.2.7).

For the next minutes the IPD-SPR extinction band increased up to 0.90 at 150min; meanwhile the OPD-SPR band at 400nm decreased until almost disappearing, meaning

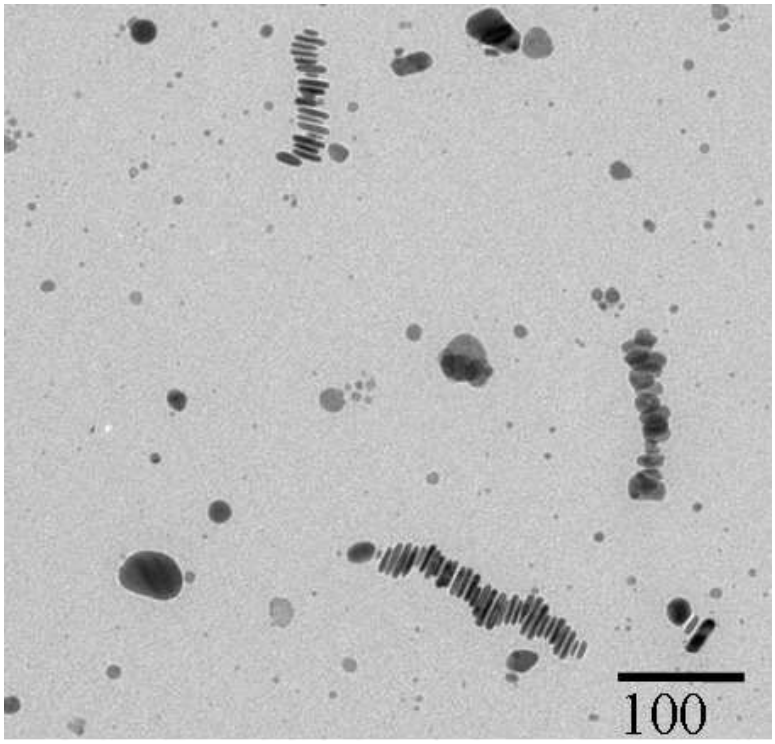

Figure 4.2.6: TEM image of sample A2 at 45 minutes of green light irradiation. Flat rounded nanoparticles with a mean size of size 21±0.8nm were the dominant morphology. The average thickness for the flat NPs was 7±3nm. Some twin and flat triangular NPs were still present in this stage of the synthesis.

that most of the seeds were transformed into other morphologies. The TEM images at the end of the synthesis showed that twin, triangle, and seed nanoparticles diminished drastically; then disks and flat rounded are the main morphologies observed (mean size 21±6 and 7±2nm thickness), see Fig. 4.2.8. Green light irradiation allows the formation of rounded flat particles; however, the right conditions for a reproducible synthesis were not completely obtained. Our hypothesis is that the plasmon band of the precursor solution (400nm) and the green light (520nm) were off resonance, which caused slow growth during the first 30 minutes; after that, the plasmon band shifted to around 690nm, and the green radiation and plasmon band remained off resonance until the end

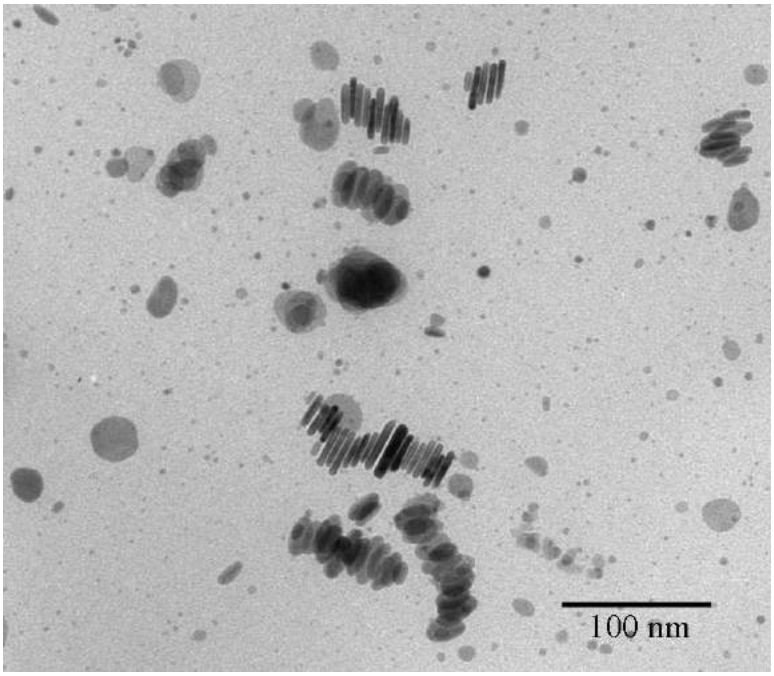

Figure 4.2.7: TEM image of sample A2 at 75 minutes of green light irradiation. Twin and seed nanoparticles were diminished drastically and flat rounded NPs with 23±6nm mean size and 6±2nm thickness were the dominant particles.

of the synthesis. This growth behavior made it hard to control the size and morphology of the particles, yielding poor reproducibility of the synthesis [34]. For this reason, the idea of combining two wavelengths was explored for the photochemical transformation of silver nanoparticles.

4.2.3 Light Assisted Transformation Combining Blue and Green Radiation

The UV-Vis optical extinction spectra of the precursor solution under blue and green radiation are shown in Fig. 4.2.2; the spectra revealed different growth kinetics of nanoparticles during the photochemical synthesis. The kinetics of the synthesis and the resulting

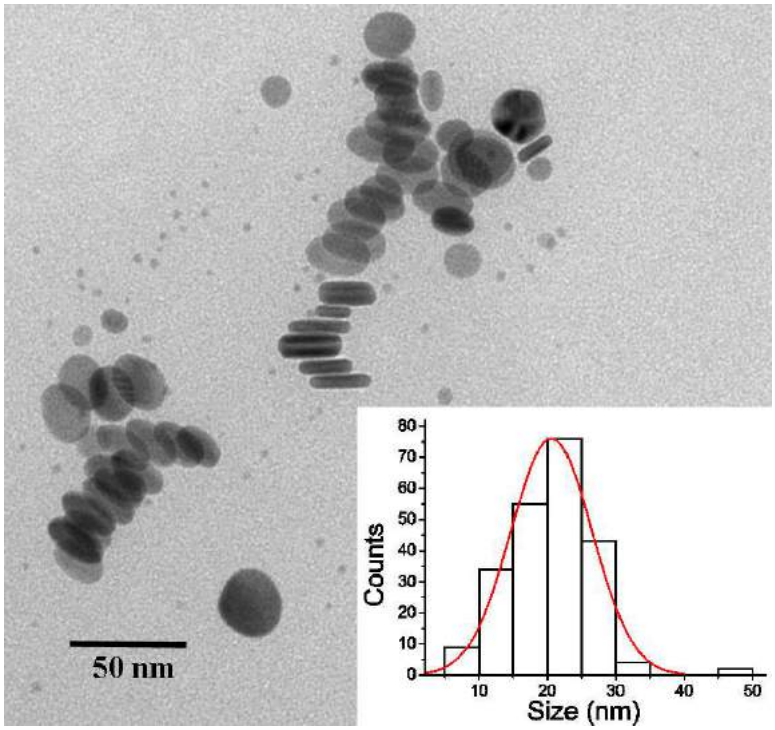

Figure 4.2.8: TEM image (A) and size distribution (B) of sample A2, synthesized under green radiation.

plasmon band are highly influenced by the wavelength chosen to induce the photochemical transformation: blue light produced twin particles, such as decahedral, prisms, and bi-pyramidal nanoparticles, while green light allowed the formation of flat rounded particles. Moreover, the differences on the plasmon bands in samples A1 and A2 at the end of the synthesis opened the possibility of tuning the optical properties and controlling the morphology of silver particles by combining two light sources as the photochemical transformation happens. In this study, the photochemical synthesis of silver NPs was carried out by changing from blue to green radiation at different exposure times. We show that under these experimental conditions, we were able to tune the plasmon band within the spectral range from 511 to 594nm with high reproducibility. As an example of how the plasmon band was controlled, Fig. 4.2.9 shows UV-Vis extinction spectra of sample A7. In this case, the precursor solution was irradiated for 10min with blue light;

after that, we changed the colloid to green light irradiation for a period of 140min or until no significant changes appeared in the spectra.

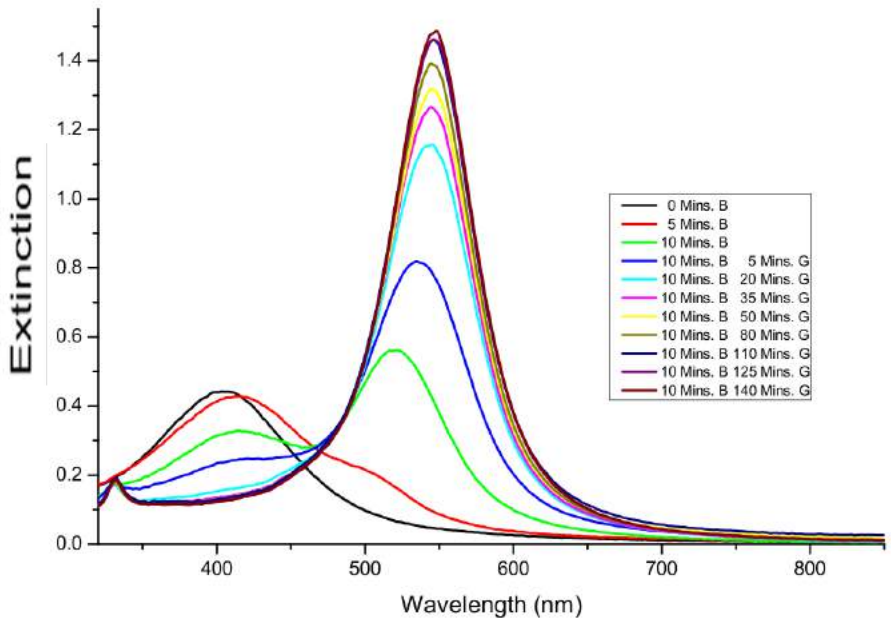

Figure 4.2.9: Kinetics of the synthesis for sample A7. The first 10min, it was irradiated with blue light (B), and then changed to green radiation (G).

We can observe that the behavior of the spectra of A7 is quite similar to those corresponding to sample A1 during the first 10min under blue light exposure (see Figs. 4.2.2A and 4.2.9): a second plasmon band appeared and the bathochromic shift was already observed. Immediately after, green radiation was used to continue the photochemical transformation. The bathocromic shift continued with fast growth in the extinction of the new plasmon band, stabilizing at 545nm; additionally, the band at 400nm, associated with seed NPs, disappeared at the end of the synthesis. The TEM images corresponding to sample A7 at the end of the synthesis showed that flat rounded nanoparticles with a mean size of 11±8nm represent the dominant morphology; some twin NPs of different sizes were also present (see Fig. 4.2.10). After 140min of continuous green light irradiation, no decahedron shaped particles were produced, and seed nanoparticles disappeared

due to the formation of bigger fiat particles.The UV-Vis extinction spectra and the TEM images showed that changing from blue to green light sources during the photochemical synthesis allowed us to control the transformation of the precursor solution and its plasmonic properties. Particularly, for the case of sample A7, the IPD-SRP band was tuned to 545nm due to the formation of flat rounded nanoparticles, see Figs. 4.2.9 and 4.2.10.

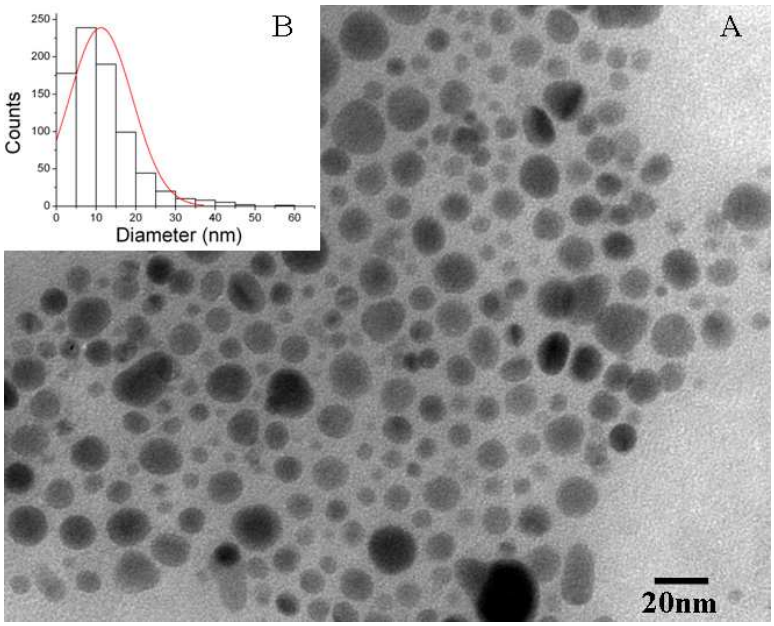

Figure 4.2.10: TEM image (A) and size distribution (B) of sample A7.

Additionally, the high tuning degree on the plasmonic bands seen in the extinction spectra of Fig. 4.2.11 was obtained by exposing each sample of the set to blue irradiation for different times, followed by green radiation (preparation details are shown in Sect. 4.1). This allowed us to tune the plasmon band from 511 to 594nm. Figure 4.2.12 summarizes the results of the photochemical transformation for the entire set of samples, showing the behavior of the IPD-SPR band at the end of the synthesis, e.g., when the silver precursor solution is exposed only to blue light, the plasmon band is located at 511nm. Nevertheless, as the exposure time of blue radiation decreases, a red shift of the IPD-SPR band is observed, exhibiting a linear behavior from 60 to 10min of blue radiation. Shorter times of blue light exposure, five minutes or less, tuned the plasmon

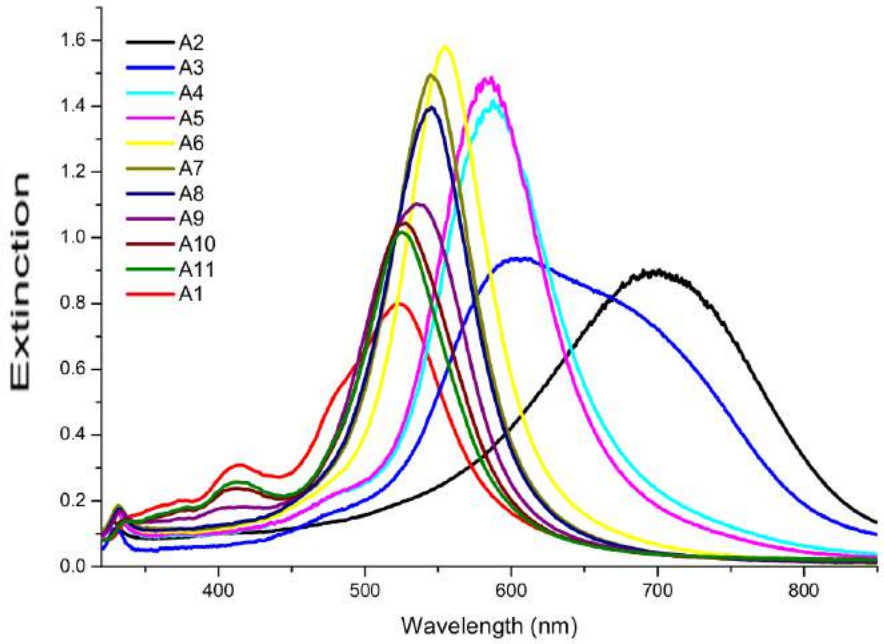

Figure 4.2.11: Extinction spectra of samples A1-A11 at the end of the photochemical synthesis.

band from 564 to 594nm, exhibiting a different behavior. Standard deviation of the plasmon band position was less than 10nm, which demonstrates high reproducibility of the photochemical synthesis.

Figure 4.2.13A shows that by irradiating the precursor solution for 5min with blue radiation, followed by 145min under green radiation (sample A6), flat rounded NPs with a mean size of 11±7nm were produced. The TEM image of sample A8 shows that elongated NPs (peanut-like) were produced when the blue exposure was set to 15min; also, some twin NPs were present in this sample. In sample A9, the number of twin NPs formed increased when the precursor solution was irradiated for 30min with blue light. In this case, faceted disks were the prevalent morphology, with a mean diameter of 42±11nm, and a few decahedral appeared. After 45min of blue light irradiation (sample A10), the nanodisks almost disappeared, and decahedra were produced with high efficiency. Therefore, by exposing the silver precursor solution to blue and green radiation, and

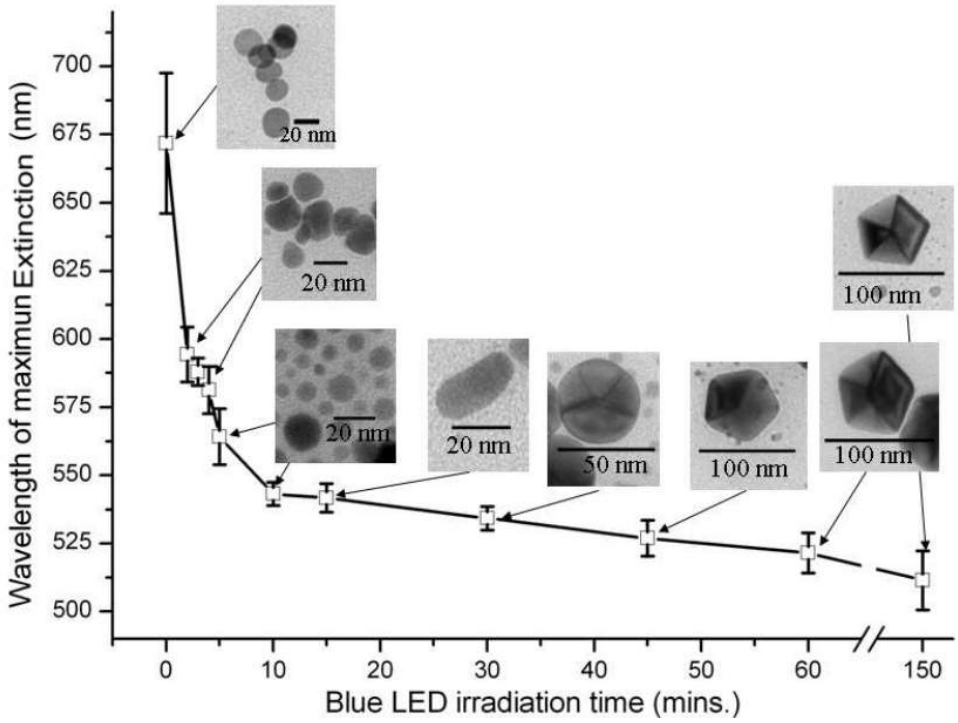

Figure 4.2.12: Position of the IPD-SPR band as a function of blue LED irradiation time. Error bars indicate the standard deviation calculated using the three different batches of samples. The inserted images show examples of the predominant morphology on each sample.

by varying the exposure times, we were able to control the morphology, going from flat rounded, flat elongated (peanuts), twin disk to decahedral, and managing to tune the IPD-SPR band from 511 to 594nm. For more details on the results and synthesis conditions, Table 4.2.1 summarizes the exposure time of blue irradiation, the final position of the IPD-SPR, the mean size of the NPs, and its dominant morphology.

Even with the differences in size and morphology, all these silver NPs are impressively stable. Samples prepared more than a year ago, stored at room conditions, have maintained their optical properties and morphology. Due to their remarkable stability and the high tuning capability of the IPD-SPR, these particles are suitable for optical applications like biosensors, plasmonics, photovoltaics and nonlinear optics. Silver NPs can

Table 4.2.1: Details of the synthesis, UV-Vis extinction spectra and TEM analyzes.

Sample	Blue irradiation time min	Plasmon Band nm	Size nm	Morphology
Ag-solution	–	400±5	3±1	Spherical
A1	150	511±11	78±13	Decahedral(sharp corners)
A2	0	677±26	21±6	Flat rounded
A3	2	594±10	24±8	Flat rounded
A4	3	588±5	24±8	Flat rounded
A5	4	581±9	24±8	Flat rounded
A6	5	564±10	11±7	Flat rounded
A7	10	543±4	11±8	Flat rounded
A8	15	541±5	17±10	Flat elongated
A9	30	534±4	42±11	Flat elongated & decahedral(circular)
A10	45	527±8	71±8	Decahedral(round corners)
A11	60	521±7	74±8	Decahedral(sharp corners)

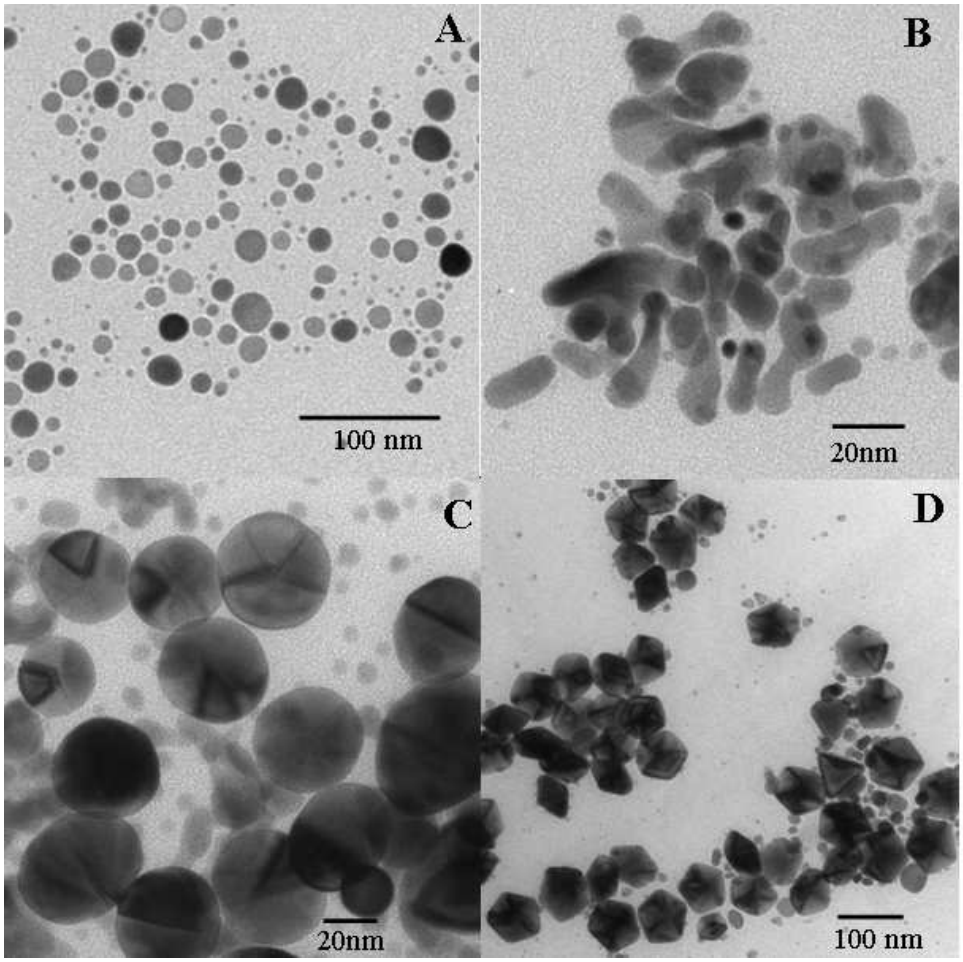

Figure 4.2.13: TEM images of the different morphologies obtained during the photochemical synthesis. Samples A6 (panel A), A8 (B), A9 (C) and A10 (D).

serve as an effective substrate for surface-enhanced Raman scattering (SERS), making it possible to detect analytes at concentrations several orders of magnitude lower than in normal Raman spectroscopy. As an example, a drop of 4-Aminothiophenol (4-ATP) $1x10^{-3}$M was allowed to dry in air at room temperature on the surface of an aluminum substrate; the mean normalized Raman spectra is shown in Figure 4.2.14A. Even at this concentration, only five characteristic Raman peaks were identified [77]. When we acquired the Raman spectra of a $1x10^{-7}$M 4-ATP sample only two very tiny peaks are

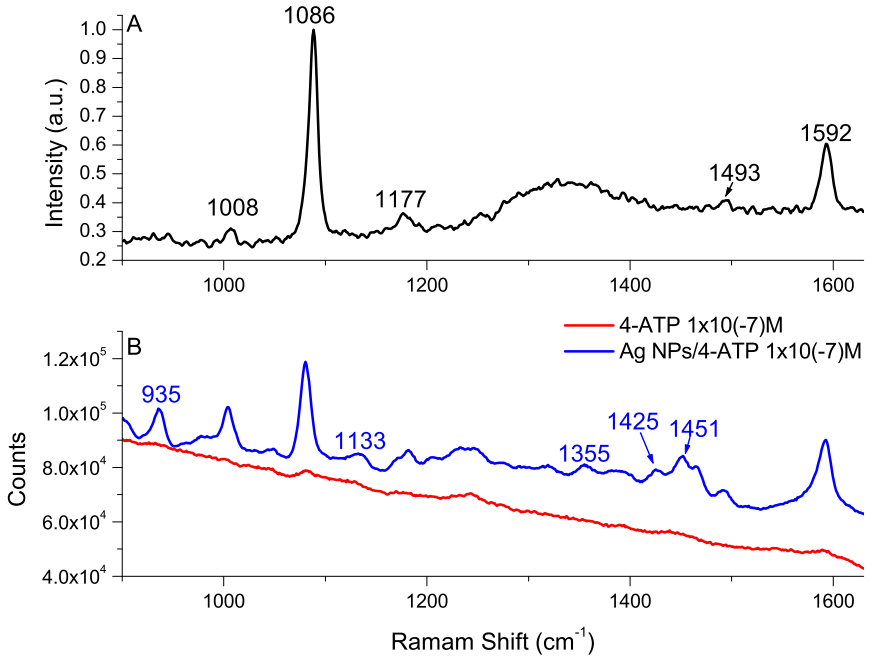

Figure 4.2.14: Normalized Raman spectrum of 4-ATP 1x10^{-3}M (panel A). Raman spectra of 4-ATP 1x10^{-7}M and the Ag NPs/4-ATP 1x10^{-7}M conjugated (panel B, red and blue respectively).

visible at 1086 and 1599cm^{-1} (red curve in Fig. 4.2.14B).

For SERS analysis, 2ml of sample A1 were cleaned by centrifugation three times at 6000rpm, the precipitate was redispersed in 100μl, and then mixed in equal volumes with a 4-ATP 1x10^{-7}M solution. A drop of this mixed solution was dried on the surface of the aluminum substrate and the Raman spectra was acquired, in this case the signal was strongly enhanced (blue curve Fig. 4.2.14B). In fact, we were able to see some weak Raman peaks located at (1133, 1355 and 1425cm^{-1}), which were not detected by the normal Raman approach at higher concentration (Fig. 4.2.14A); also, two peaks (935 and 1451cm^{-1}) assigned to PVP were enhanced [78].

Another promising application of nanomaterials is related with the enhanced light

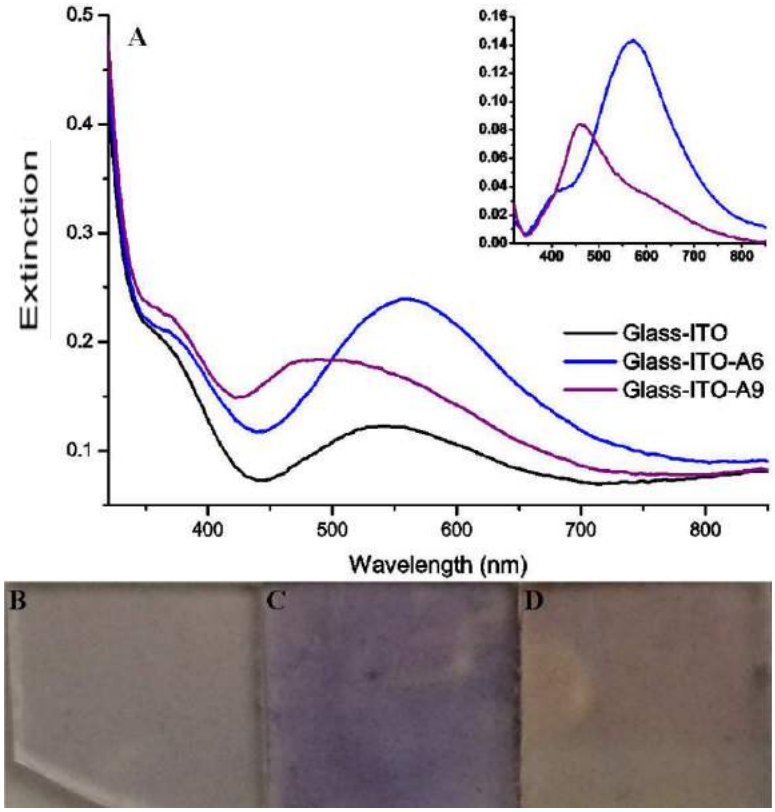

Figure 4.2.15: UV-Vis extinction spectra of glass-ITO and glass-ITO-Ag NPs substrates (Panel A) and optical images of the substrates: glass-ITO (B), glass-ITO-A6 (C) and glass-ITO-A9 (D).

harvesting using plasmon-resonant metal nanoparticles, because the redistribution of electromagnetic field modes around the metal particles enhances absorption, scattering or optical emission. For example, metallic nanoparticles (spherical, prisms, rods) have been tested to enhance the performance of the bulk heterojunction organic photovoltaic (OPV) solar cells; the particles can be integrated into the active layer or between the interfaces of the active and contact layers (cathode and anode) to increases light absorption. Here, we have shown that our flat silver nanoparticles can be deposited on surface of glass substrates coated with Indium tin oxide (ITO) for its possible application in organic solar cells. ITO coated glass substrates were sonicated for 10min in acetone, and

two times in iso-propanol. The glass substrates were thoroughly rinsed with miliQ water. Immediately after, they were immersed for 24 hours in a 3% (3-Aminopropyl)trimethoxysilane (APTMS) in methanol solution for substrate activation. Activation with APTMS causes the presence of amine groups on the substrate surface, which can electrostatically attach with the Ag NPs. After the substrates were sonicated three times in methanol, they were dried with cleaned compressed air. The activated ITO/glass substrates were immersed overnight in the Ag NPs colloids, samples A6 and A9 respectively. Finally, both substrates were washed with plenty of Milli-Q water and dried with cleaned compressed air. Optical images and UV-Vis extinction spectra were recorded for glass-ITO, glass/ITO/A6 and glass/ITO/A9. The corresponding optical images of the three substrates are shown in Fig. 4.2.15, panels B, C and D respectively; as it can be seen, in both cases a uniform layer of Ag NPs was deposited onto each substrate. The UV-Vis spectra reveal that glass-ITO substrate has only one absorption peak in the spectral region of the maximum emission of solar radiation, around 544nm, with a maximum absorbance value of 0.12. While in the case of glass/ITO/A6, the extinction band becomes broadening, and the maximum extinction is located at 560nm with an extinction value of 0.24, almost the double of the previous case. For the latter case, glass/ITO/A9, the maximum extinction is centered around 490nm, with a maximum extinction of 0.18. Our preliminary results show that silver particles coated with PVP can be easily deposited on the silanized surface of glass coated with ITO; the optical extinction can be modified by selecting one of samples produced through photochemical synthesis. The inset of figure 4.2.15A shows the UV-Vis optical extinction spectra of samples A1 and A9 acquired with glass/ITO as a reference background.

4.3 Conclusions

It was noted that the resulting plasmon band is highly influenced by the wavelength chosen to induce the photochemical transformation: blue light produced twin particles,

such as decahedral, prisms, and bi-pyramidal nanoparticles, while green light allowed the formation of flat rounded particles. Moreover, the UV-Vis optical extinction spectra revealed different growth kinetics of nanoparticles during the photochemical synthesis; the differences on the plasmon bands in samples synthesized with blue and green LEDs opened the possibility of tuning the optical properties and controlling the morphology of silver particles by combining two light sources as the photochemical transformation happens. We made a study in which the photochemical synthesis of silver NPs was carried out by changing from blue to green radiation at different exposure times. The results showed the high tuning capability of the IPD-SPR band of silver nanoparticles, which results in different NP morphologies through the photochemical transformation of silver precursor solutions, these results are presented in Section 4.2. By means of a simple one-pot, two-step light assisted process, it was possible to transform small spheres in the precursor solutions into flat rounded, flat elongated, twin disks, and decahedral NPs. In addition, photochemical transformation with the use of two light sources, blue and green LEDs, allowed us to select the IPD-SPR band with high tuning accuracy, from 511 to 594nm, by simply controlling blue irradiation time. This is a fast and low cost method that allows tuning the IPD-SPR band within a wide region of the visible spectrum, and it could be escalated to farther regions of the IR with the use of longer wavelength light sources. Besides, we showed some preliminary results of two promising applications of the photochemical produced Ag NPs. The first of them is the use of Ag decahedral NPs as a SERS substrate; by a simple solution-mixing and drop-casting method it was possible to detect a $1x10^{-7}$M concentration of 4-ATP, this is a concentration four orders magnitude less than the detected by normal raman. In the second possible application, we showed that the flat rounded and the rounded decahedral NPs can be deposited into a glass-ITO substrates for their use in organic photovoltaics.

CHAPTER 5

Functionalization of Silver and Gold NPs

Functionalization is the modification by adding or replacing chemical species in the surface of a material. By selecting the appropriate chemical species in the surface of the NPs it is possible to control their interaction with other materials or with other nanoparticles. A proper functionalization is important because most of the optical properties of the metallic NPs are surface and distance dependent; in biological applications the functionalization or surface coating of the NPs plays a principal role in the interaction of these materials and the biological systems.

This Chapter will present the results obtained in the functionalization of silver and gold NPs. The Ag decahedral NPs were functionalized to make them biocompatible, expecting to reduce the silver cytotoxicity, details on this can be found in Section 5.1. Section 5.2 presents the introductory results on gold nanoparticles functionalization aimed to have a good biocompatibility in cell cultures. These results were a first approach in the nanoparticles-cell interactions and the experiments were focused in the study of the cytotoxicity of the nanoparticles capping molecules.

5.1 Functionalization of Ag Decahedral NPs

5.1.1 Methods

First a solution containing 10% wv BSA in milli-Q water and a solution of 4-ATP 5.9mM in methanol were prepared. Then 10ml of Ag decahedral nanoparticles were prepared as described in Subsection 3.1 using PVP as surfactant. One day after the NPs were prepared, 200μl of BSA and 240μl of 4-ATP were added under rapid magnetic stirring and the solution was left to react for one day. Finally the decahedral+4-ATP+BSA solution was cleaned using a dialysis membrane (12-14kD) in order to remove the non-attached 4-ATP and the synthesis residues. The samples were washed in Milli-Q water with vigorous stirring for 48 hours, changing the water every 8 hours.

5.1.2 Results

Silver decahedral NPs plasmon band is very close to a very common laser band (532nm), which makes this morphology very suitable for diverse optical applications. Decahedral NPs were synthesized and functionalized as described in Section 5.1.1 in an attempt to make them biocompatible, since we wanted to study their interaction with cell cultures. We also wanted to remove the PVP present in the colloidal solution and the synthesis residues to avoid interactions non-related with the Ag NPs in these cell cultures.

Upon the adding of the BSA and 4-ATP the sample was stable for several days, but when dialized in order to remove the PVP, the non attached 4-ATP and synthesis residues the colloidal stability was compromised; most of the NPs were lost by agglomeration or by adhesion to the dialysis membrane, it can be noted by the reduction in the extinction in Fig. 5.1.1. It was not possible to redisperse the agglomerated NPs or to de-attach them from the membrane. It was noted from the previous experiments that there is a determined amount of PVP that can be removed (by dialysis or centrifugation) from the colloidal solutions before they agglomerate, making impossible to redisperse the Ag NPs again. We expected that the functionalization with 4-ATP and BSA will help the colloidal

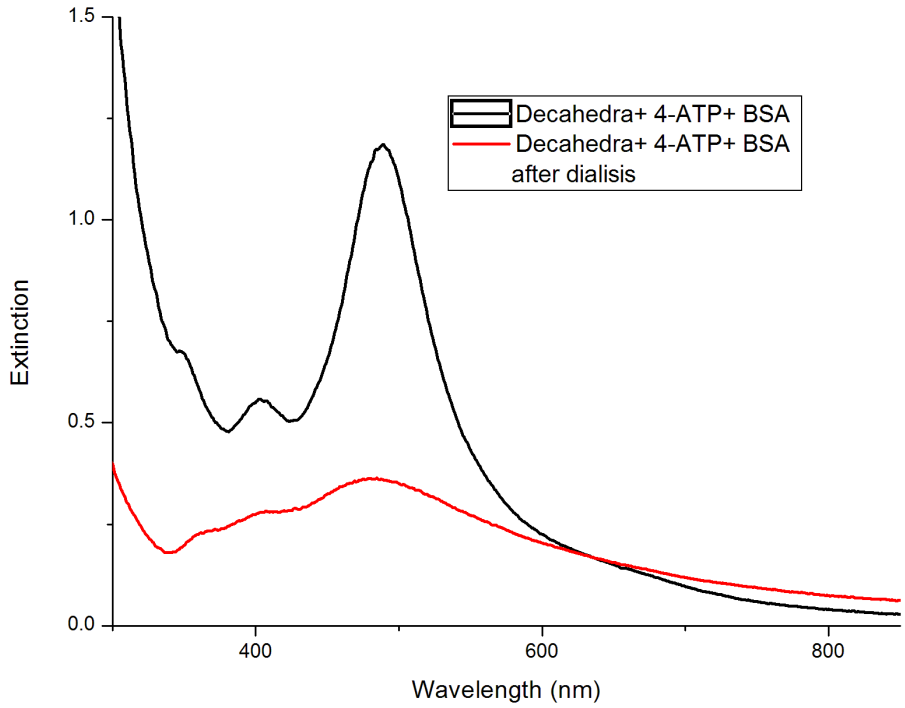

Figure 5.1.1: Functionalized decahedral NPs UV-Vis spectra before and after been cleaned by dialysis.

stability and will let us remove the PVP, unfortunately this not happened. Future studies will be focused in solving all these problems in order to study the interaction of these functionalized Ag NPs with some cancer cell lines.

5.2 Synthesis and Functionalization of Gold NPs and their Interaction with HeLa Cell Cultures

From the results obtained in Section 5.1.2, we observed that the proposed functionalization route was not suitable for Ag NPs. Nevertheless, we decide to apply this procedure of functionalization to gold NPs. The choose to functionalize gold nanospheres was based in the fact that this is the most common morphology used in cytotoxicity assays, and by this we can compare our functionalization method with the results available in the literature.

5.2.1 Methods

Synthesis and functionalization of Gold NPs

Gold nanorods: The synthesis of gold nanorods (GNRs) was done using the method previously reported by Nikoobakht and El-Sayed[4]; in this method a seed solution of spherical NPs is added to a growth solution including Au, CTAB and silver nitrate and reduced with ascorbic acid. The seed synthesis was done by mixing 2.5ml of 0.5mM $HAuCl_4$ and 2.5ml of 0.2M CTAB solution at room temperature, the solution was magnetically stirred and 0.5ml of ice cold 10mM sodium borohydride was added. Stirring continued for 5 minutes and the solution turned brownish color. The seed solution was left undisturbed for half an hour. The growth solution was made by mixing 10ml of 0.2M CTAB, 10ml of 0.5mM $HAuCl_4$, 130μl of 10mM silver nitrate and 90μl of 0.1M ascorbic acid under vigorous stirring. Finally 240μl of the seed solution was added to the growth solution and after some minutes the color changed to a red tone. After that the colloids were washed by centrifugation at 6500 RPM for 30min and the precipitate was redispersed in Milli-Q water. For the silica coating of the gold nanorods, 20ml of the redispersed rods were placed under a reflux beaker at 30^{o}C, then 0.20ml of NaOH 0.1M were added under slow magnetic agitation and the reflux beaker was sealed [8, 79]. After

20 minutes 60μl of 20% TEOS in methanol was injected, followed by two other injections at 30min intervals. After 6 hours the solution was taken out of the beaker and centrifugated at 6500RPM for 30mins, two times in ethanol and one time in water. Finally the precipitate was redispersed in Milli-Q water. This allowed us to have a silicacoated GNRs suspension with good colloidal stability (labeled as GNPs I).

NPs coated with 4-ATP: The synthesis of 4-ATP-coated gold nanoparticles (labeled as GNPs II) was done by dissolving 198μl $HAuCl_4$ (253mM) in 50ml of Milli-Q water, then 10μl of 4-ATP (5.9mM) and 0.5ml of ice cold $NaBH_4$ (0.1M) were added sequentially under vigorous magnetic agitation; the solution changed to a bright red color when the $NaBH_4$ was added.

NPs coated with cysteamine: For the synthesis of cysteamine-capped gold NPs (labeled as GNPs III), 198μl of $HAuCl_4$ (253mM) were added to 50ml of Milli-Q water under vigorous stirring, then 10μl of 5.9mM cysteamine and 0.5ml of ice cold sodium borohydride (0.1M) were added sequentially. Upon the addition of sodium borohydride the solution turned into a bright red one.

NPs coated with cysteamine and BSA: For the stabilization with BSA (labeled as GNPs IV), 2ml of 10% wv BSA were added to 20ml of the as prepared cysteamine-capped NPs.

Purification of the functionalized nanoparticles: In order to remove the non-attached bio-molecules and synthesis residues, the four samples were cleaned using a dialysis membrane (12-14kD). The samples were washed in Milli-Q water with vigorous stirring for 48 hours, changing the water every 8 hours. Finally, the optical extinction in the peak of maximum extinction was adjusted to 1.0 OD with adding of Milli-Q water for the four gold NPs, resulting in a gold concentration of $2.47x10^{-4}$M silica-capped GNRs, $3.14x10^{-4}$M for the 4-ATP-capped and $2.77x10^{-4}$M for the cysteamine- and cysteamine-BSA-capped GNPs.

Hela Cell Cultures

The human cervix cancer cell line HeLa ATCC®. CCL-2™was selected for this study. The cells were cultivated in DMEM (Dulbecco's Modified Eagle's Medium, GIBCO, USA) supplemented with fetal bovine serum 10% (GIBCO, USA) and incubated at 37°C, 5% CO_2.

Exposure of HeLa Cells to GNPs

HeLa cells cultures (4x10^5 cell/100μL) were prepared in 96-well plates (Costar, Corning, USA), which were exposed to GNPs 5μl for 24hrs. The resulting gold concentration in the cell cultures was 12.4μM for the silica-capped GNRs, 15.7μM for the 4-ATP-capped and 13.9μM for the cysteamine- and cysteamine-BSA-capped GNPs. The cells were exposed to NPs in two cases: **A)** GNPs added at the time of subcultivation (0hrs) and **B)** GNPs added at the time that monolayer cells were 70% confluent (24hrs after subcultivation).

Cell Viability Determination

Trypan Blue exclusion which can be used to discriminate between viable (unstained) and non-viable cells (blue stained). The cells were exposed to GNPs as previously described. After exposure, 0.4% Trypan Blue solution (1:10 dilution) was added and incubated by 3min. The viable cells were counted in Neubauer chamber used an inverted microscopy (Carl Zeiss).

Metabolic Activity Determination

The XTT assay is a colorimetric assay that detects the cellular metabolic activities. During the assay, the yellow tetrazolium salt XTT (2,3-bis (2-metoxi-4-nitro-5-sulfofenil)-2-h-tetrazolium-5-carboxanilide) is reduced to a highly colored formazan dye by dehydrogenase enzymes (mitochondria) in metabolically active cells [80]. The cells were exposed to GNPs as previously described. After exposure, 100μL of XTT detection solution

(0.25mg/mL in 0.1mM Menadione, Sigma) were added to each well and the plate was returned to the incubator for 90min. The formazan dye formed in the assay was quantified by measuring the extinction at 450nm in a spectrophotometer (Epoch Biotek).

Genomic DNA Integrity

Cells were exposed to GNPs for 24 hours in both cases: **A)**at the time of subcultivation and **B)** monolayer cells. Genomic DNA extraction was performed according to the AxiPrepTM Multisource Genomic DNA Miniprep kit (AXIGEN Biosciences). DNA samples were analyzed on 0.8% agarose gels and stained with Gel RedTM (BIOTUM). The size marker was HyperLadderTM 1kb (BIOLINE). The bands were visualized in ChemiDoc MP System (UV light at 260-280nm, BIORAD) and image acquisition with Image LabTM software (BIORAD).

Cytoskeleton Analysis (Stained of Microfilaments Actin)

Control cells and those exposed 1h to GNPs, were fixed with 4% p-formaldehyde for 20 min, permeabilized with 0.05% Triton buffer containing 10 mM Tris, 5 mM KCl, 1 mM $MgCl_2$, and later exposed to FITC-phalloidin (Sigma Aldrich). The preparations were mounted using Vecta Shield-DAPI (4',6-diamidino-2-phenylindole) a fluorescent stain that binds strongly to A-T rich regions in DNA (Vector Laboratories, USA) and observed under a fluorescence microscope (Leica, DMLS) using a 450-490nm B filter. The images acquisition was done with camera AxioCam ICc1 (Carl Zeiss).

Statistical Analysis

Statistical analysis was performed by one-way analysis of variance. Tukey Kramer was used as a post hoc test to determine significant differences between treatments ($P<0.005$), using the commercial software JMPIN, ver 4.0.3.

5.2.2 Results

In order to have a first approximation to the NPs-cell interactions we decided to functionalize Au NPs. We studied the toxicity of silica-capped gold nanorods and gold nanospheres coated with three different organic molecules: 4-aminothiophenol (4-ATP), cysteamine, and serum bovine albumin (BSA). The gold nanoparticles were synthesized and functionalized as explained in section 5.2.1. For toxicity evaluation, cervix cancer cell line HeLa ATCC CCL-2TM was selected, and cells were incubate at the time of subcultivation (0hrs) and when the monolayer cells were 70% confluent (24hrs). Cell viability, metabolic activity, genomic DNA integrity and Cytoskeleton integrity were evaluated to elucidate the cell response to the GNPs. For more details on the cell cultures and biological assay please refer to the Section 5.2.1.

Gold Nanoparticles and Coatings

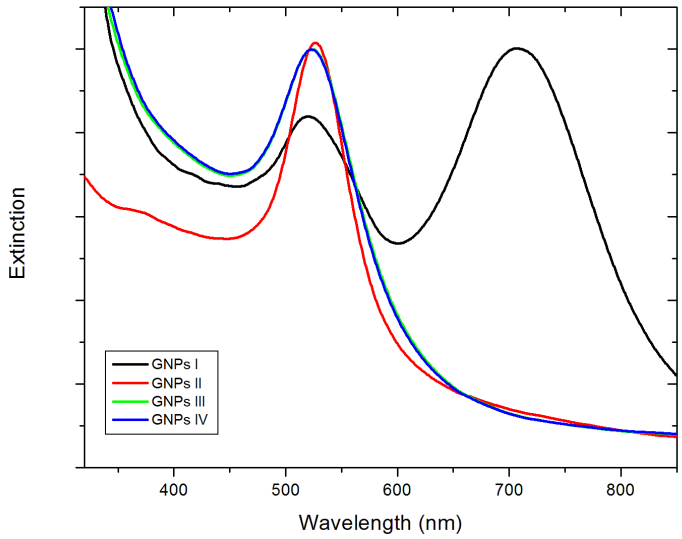

Figure 5.2.1: UV-Vis spectra for the different GNPs (I-IV): (black line) Rods-silica-, (red) 4-ATP-, (green) Cysteamine- and (blue) Cysteamine-BSA-capped GNPs.

The gold nanoparticles were synthesized and functionalized as explained in section 5.2.1. Figure 5.2.1 shows the UV-Vis optical spectra for the four GNPs, all GNPs colloids were adjusted to 1.0 OD; silica-capped gold nanorods (labeled as GNPs I) is represented by the black line, the spectrum show the characteristics two extinction bands, associated to the transversal (520nm) and longitudinal (710nm) plasmon resonances bands, due to the anisotropic morphology of the nanorods. TEM images revealed that nanorods have a mean size of 9±1nm in diameter, 22±4nm in length and with a porous silica shell of 10±5nm (Fig. 5.2.2a). Meanwhile, the nanospheres exhibited only one extinction band, at 526nm for the 4-ATP-capped GNPs (labeled as GNPs II), and at 524nm for both the cysteamine- and cysteamine-BSA- capped GNPs (labeled as GNPs III and IV, respectively). TEM images revealed spherical nanoparticles with a mean sizes of 34±5, 24±4 and 25±5 nm for GNPs II, III and IV, respectively (Figs. 5.2.2b, c and d).

Functionalization was studied first by means of Raman spectroscopy; Figure 5.2.3 shows the characteristic normal Raman spectra for the three biomolecules (4-ATP, cysteamine and BSA) used for the functionalization, as well as the SERS Raman spectra of the functionalized GNPs II-IV in the spectral region from 500-150cm^{-1} [77, 81–86]. Figure 5.2.3A shows the characteristic Raman spectrum of 4-ATP (80mM in methanol) where peak at 1082cm^{-1} (assignment to νCC and νCN) shows the higher intensity, some more weak intensity peaks also can be observed 640(γCCC), 829(πCH), 1006(γCC and γCCC), 1178 (δCH), and 1493cm^{-1} (νCC+ δCH). One drop of cysteamine solution (130mM in methanol) was deposited and the spectra were acquired once it dried, the most intense peak was observed about 722cm^{-1} (νCS), followed by the peak around 954cm^{-1} (νCC), also another characteristic but less intense peaks were observed at 642 (gauche conformer of the SCC chain), 760 (trans conformer of the SCC chain), 1265 (τCH2), 1286 (πCH2) and 1459cm^{-1}(δCH2) (Fig. 5.2.3B). Finally figure 3C shows the characteristic Raman spectra of BSA prepared in water at 10% w/v, the most intense peak is observed from 1300 to 1380cm^{-1}(CH, tryptophan), followed by 1003 (phenylalanine) and 1448cm^{-1} (δCH), some less intense characteristic peaks also can be observed.

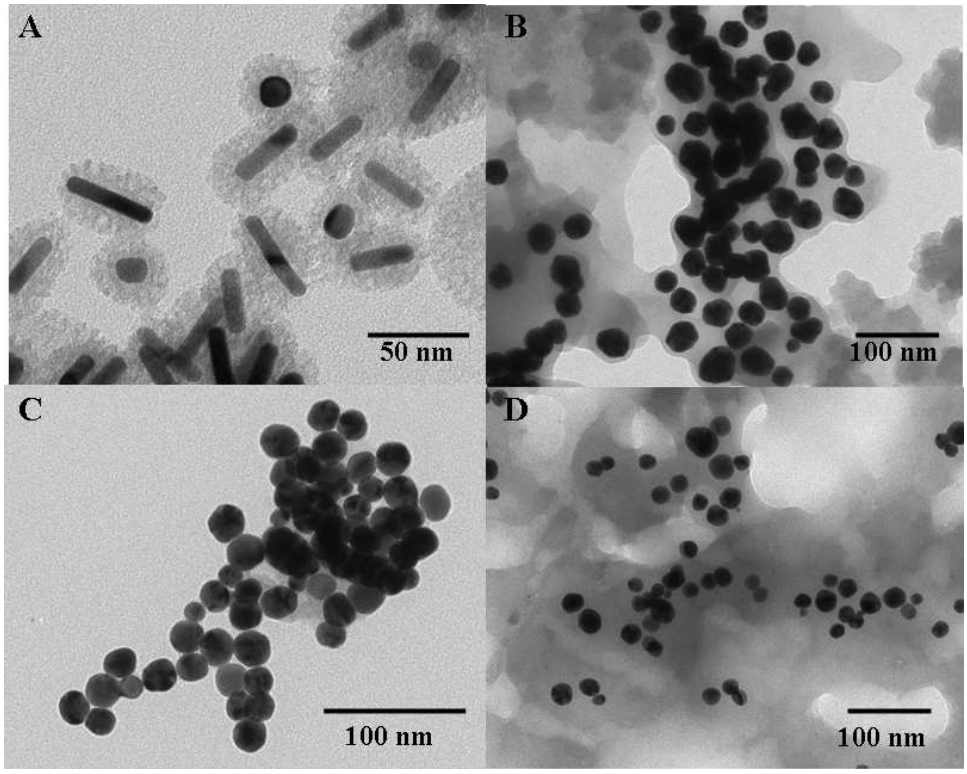

Figure 5.2.2: TEM images for the Rods-silica- (22±4 nm long, 9±1 nm wide and 10±5 nm silica shell), 4-ATP- (34±5 nm), Cysteamine- (24±4 nm) and Cysteamine-BSA-capped gold NPs (25±5 nm) (panels A-D respectively).

Meanwhile the SERS spectra of the functionalized GNPs are shown in the right side of figure 5.2.3, the SERS spectra of GNPs II (with a concentration of 4-ATP of 47.2x 10^{-6}M, fig. 5.2.3D) shows some of the characteristic peaks of 4-ATP but now with a different relative intensities, the peak at 1082cm^{-1} still exhibits the highest intensity, however the intensity of peaks at 1178 and 1493cm^{-1} were enhanced more than the rest of the peaks, besides new peaks were observed, one of them at 557 (γCCC), 635 (δCH) and 1141cm^{-1} (δCH), the last two peaks are attribute to the oxidative transformation of 4-ATP into 4,4'-dimercaptoazobenzene(DMAB) [86]. On the other hand, the SERS signal from GNPs III was not as strong as in the case of GNPs II; one of the most notorious spectral characteristic was the peak at 722cm^{-1} which is very strong in normal

Raman, but almost disappeared in SERS. The relative intensity of the strong peaks in the cysteamine sample were diminished in the GNPs III, but some weak peaks that were not visible in normal Raman, now can be seen in the GNPs III SERS spectrum (Fig. 5.2.3E). GNPs IV, which is capped by cysteamine and BSA, showed Raman peaks from both biomolecules (Fig. 5.2.3F). The label colors in figure 5.2.3F indicates to which biomolecule the Raman peak is associated, blue for cysteamine and green for BSA.

Cell Viability of HeLa Cells Exposed to GNPs

Table 5.2.1: Cellular viability and metabolic activity of HeLa cells exposed to GNPs I-IV. The GNPs were placed **A)** at the time of subcultivation and **B)** monolayer cells with 70% confluent. The experiments were performed in triplicate and the data are expressed as cell viability and metabolic activity percentage.

	Cellular viability/Metabolic Activity	
GNPs	A)At the time of subcultivation (0hrs)	B) Monolayer cells (24hrs)
I	92/108	90/73*
II	99/95	99/87
III	99/110	93/86
IV	99/108	100/97

*Statistically different from the control unexposed HeLa cells ($p<0.05$).

All the biological assays presented in the next sections were performed in the Dr. Myrna Sabanero's Lab at Guanajuato University, for which I'm deeply grateful.

For the cell viability assessment, trypan blue exclusion assay was performed to determine the cytotoxicity of GNPs, see Table 5.2.1. Cells that could easily uptake the dye were considered to be unviable while cells that excluded the dye were counted as viable.

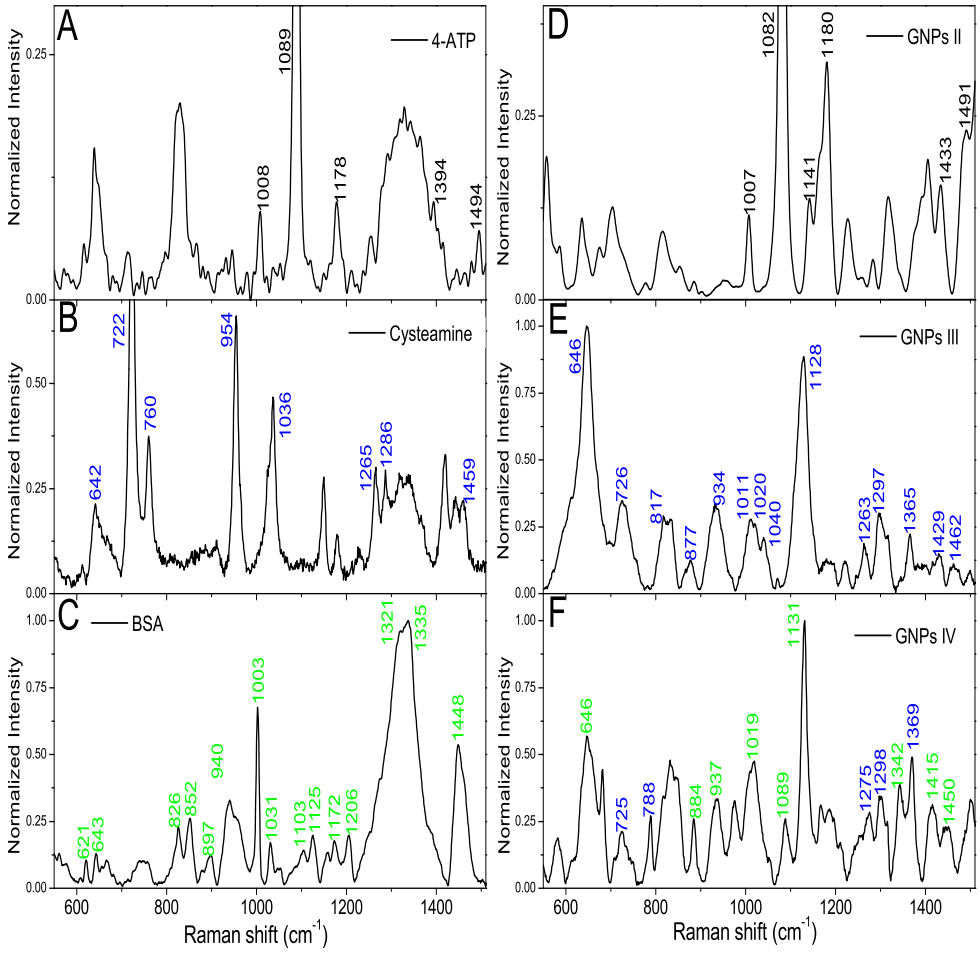

Figure 5.2.3: Raman spectra of the organic biomolecules are shown in the left column and GNPs II-IV in the right column. Band assignment was taken from references [77, 81–86] denoting: ν; stretch, δ and γ; bend, π; wagging, τ; torsion. For the case of the GNPs spectra, the color of the labels indicates to which biomolecule the band is associated to: black for 4-ATP, blue for cysteamine and green for BSA.

The experiments were performed in triplicate and the data is expressed as cell viability

percentage. Table 5.2.1 shows the corresponding results of cell viability for both cases of exposure: **A)** GNPs added during subcultivation (at 0hrs) and **B)** GNPs added when the monolayer cells was 70% confluent (24hrs). For the case of GNPs I, we observed a small reduction in the viability, 93 and 90% respectively for **A)** and **B)**; the result was unexpected, because in some reports they shown that CTAB, which is highly toxic for cells, because it cannot be eliminated for full from gold nanorods, then is expected that gold nanorods coated with porous silica still cause toxic effects in the cells. For GNPs II, those capped by 4-ATP, viability was 99% for both cases of exposure; this result indicates that 4-ATP molecule is very suitable as a biocompatible coating. GNPs III, the cysteamine-capped GNPs, presented a viability of 99% for case **A)** and 93% for case **B)**, again we observed that the organic coating exhibit a good viability. Nevertheless, that GNP III, for case **B)** showed the lower viability, a surprising result was observed when BSA is added to the cysteamine-capped GNPs, meaning GNPs IV, the viability raised almost 100% for both cases of exposure; it seems that BSA increases the viability significantly. Figure 5.2.4 shows the microscopy images of HeLa cells after the exposure with NPs at 24hrs, the morphology of the exposed cells to the GNPs is not significantly different from control cells (figures 5.2.6 and 5.2.7, panel A), this is due to the low toxicity of the organic molecules, besides the microscopy images show some agglomerates of GNPs inside the cells, indicated by the red arrows, and they are localized outside of the nucleus.

Metabolic Activity of HeLa Cells Exposed to GNPs

The comparative metabolic activity of the cells incubated with different GNPs (I-IV) by the two exposure cases is shown in Table 5.2.1. When the GNPs were added at the time of subcultivation, the metabolic activity is in the same range as the control for the four GNPs. Moreover, this result indicates that adding the GNPs at the time of subcultivation did not alter the cell adhesion. On the other hand, when the GNPs were added to the monolayer cells the metabolic activity decreased for the GNPs I-III. Metabolic activity of

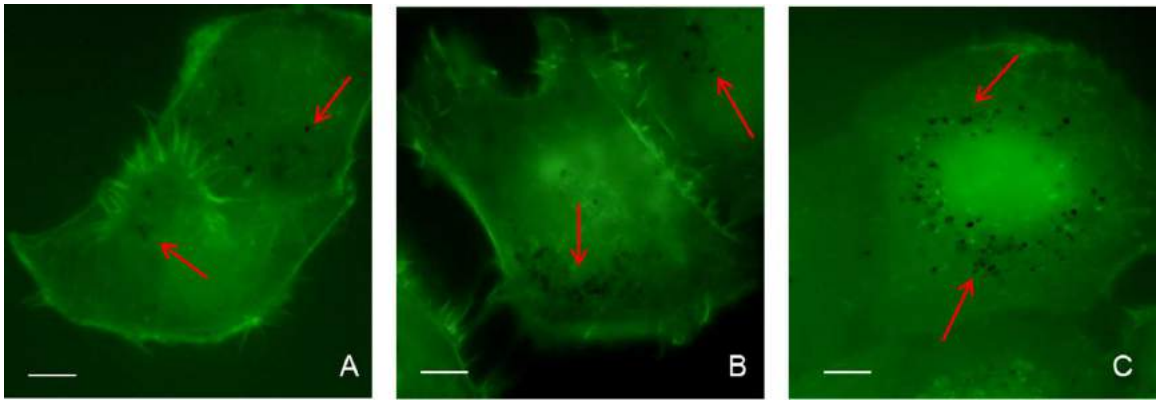

Figure 5.2.4: The GNPs II-IV were placed in monolayer cells for 1h (A-C). The F-actin-microfilaments were stained with Phalloidin-FITC, arrows indicate the GNPs aggregates detected for GNPs II-IV. Scale bar is 20μm.

cells incubated with GNPs I was 73%, and cells exposed to GNPs II and III also exhibit lower metabolic activity respect of the control cells, 87 and 86% respectively. While GNPs IV added to the cells, seems that the metabolic activity of them were not altered in any of the two exposure cases, the measured metabolic activity was 108 and 97% respectively. Then, confluent cells at 70% incubated with GNPs I shown the lowest metabolic activity register. Although it is not clear why it happened, our hypothesis is that the uptake of GNPs by the HeLa cells is sensitive to the time they are added; for example, at time 0hrs, exposure case **A)**, GNPs are distributed homogeneously in the culture medium and cells are just over the surface of the substrate (not fixed in the substrate yet), and if sedimentation of GNPs can take place, the local concentration of GNPs changes slightly in cell uptake. While for the exposure case **B)**, where the cell monolayer have covered the 70% of the surface, GNPs are distributed homogeneously in the culture medium, but if sedimentation occurred, they settle over the cell monolayer and the probability of penetration increases, causing that the metabolic process can be modified by the rising number of GNPs inside the cells. Our hypothesis was not probed, and then additional test should be carried out in order to probe it, which we are considering in a future work.

Genomic DNA Integrity

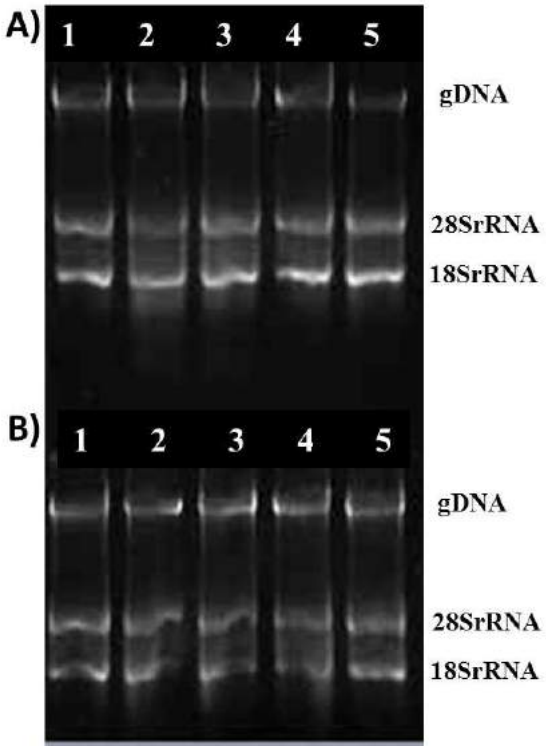

Figure 5.2.5: Genomic DNA of cells exposed to GNPs at the time of sub-cultivation (A) and monolayer cells (B). Control (Lane 1); HeLa cells culture exposed to GNPs I-IV (Lanes 2-5).

Figure 5.2.5 show the image of the gel electrophoresis for the genomic analysis of DNA. Lane 1 shows the band for the non-exposed control cells. No alterations of DNA structure after treatment with either GNPs of "'I-IV"' (Figure 5.2.5, lanes 2-5) was shown for both exposure cases, moreover the rRNA bands, 28S and 18S, were visualized, then we can conclude that gold nanoparticles coated with organic molecules did not cause genotoxic damages.

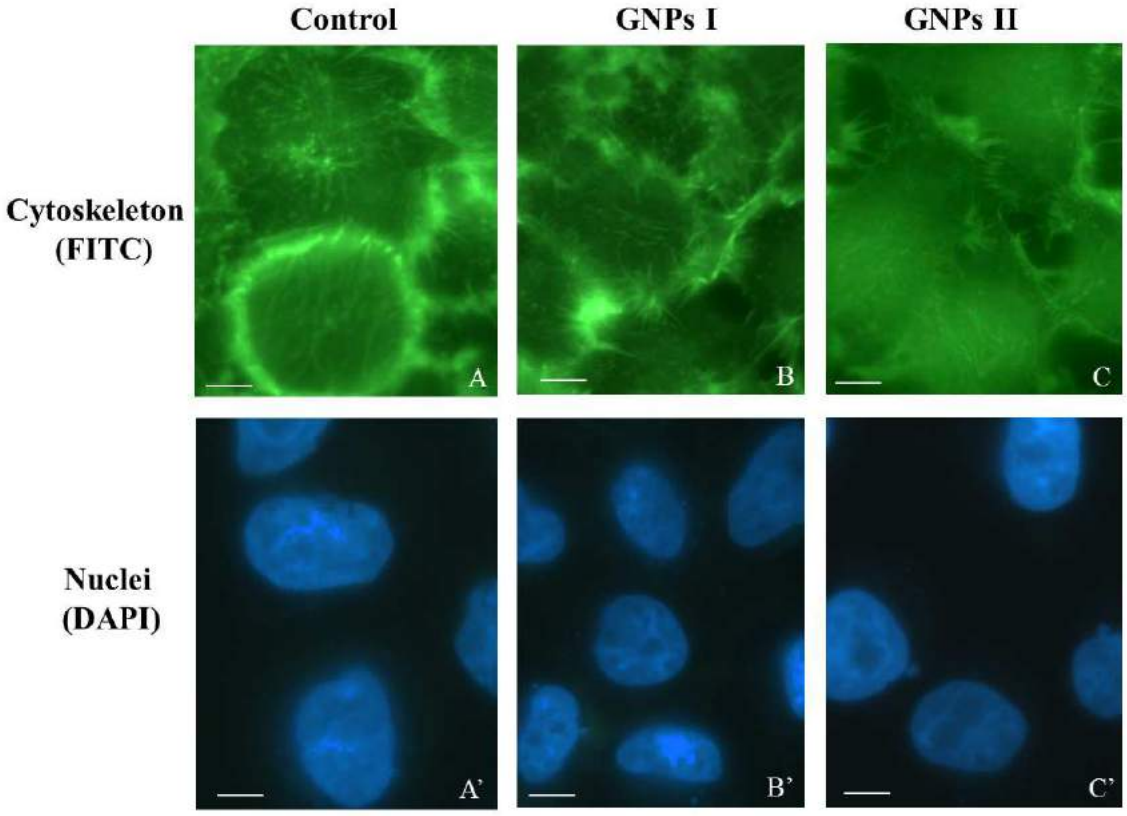

Figure 5.2.6: Effect of GNPs I and II on the cytoskeleton of HeLa cells. The control cells were unexposed to GNPs (A, A'). The GNPs were placed in monolayer cells for 1h (B-C and B'-C). The F-actin-microfilaments were stained with Phalloidin-FITC and the nuclei with DAPI. Scale bar is 10μm.

Cytoskeleton Analysis

Another important factor for the evaluation of toxicity of gold NPs is the evaluation of the cytoskeleton. The cytoskeleton is composed mainly by protein filaments called molecular motors (microfilaments, microtubules, and intermediate filaments), which form a three dimensional mesh work and they are very important in regulating endothelial cell structure and function. Modification or destruction of these molecular motors caused significant physiological, functional and morphological changes of cells, and even cell death. It is important evaluate if the interaction of GNPs can cause any damage to the

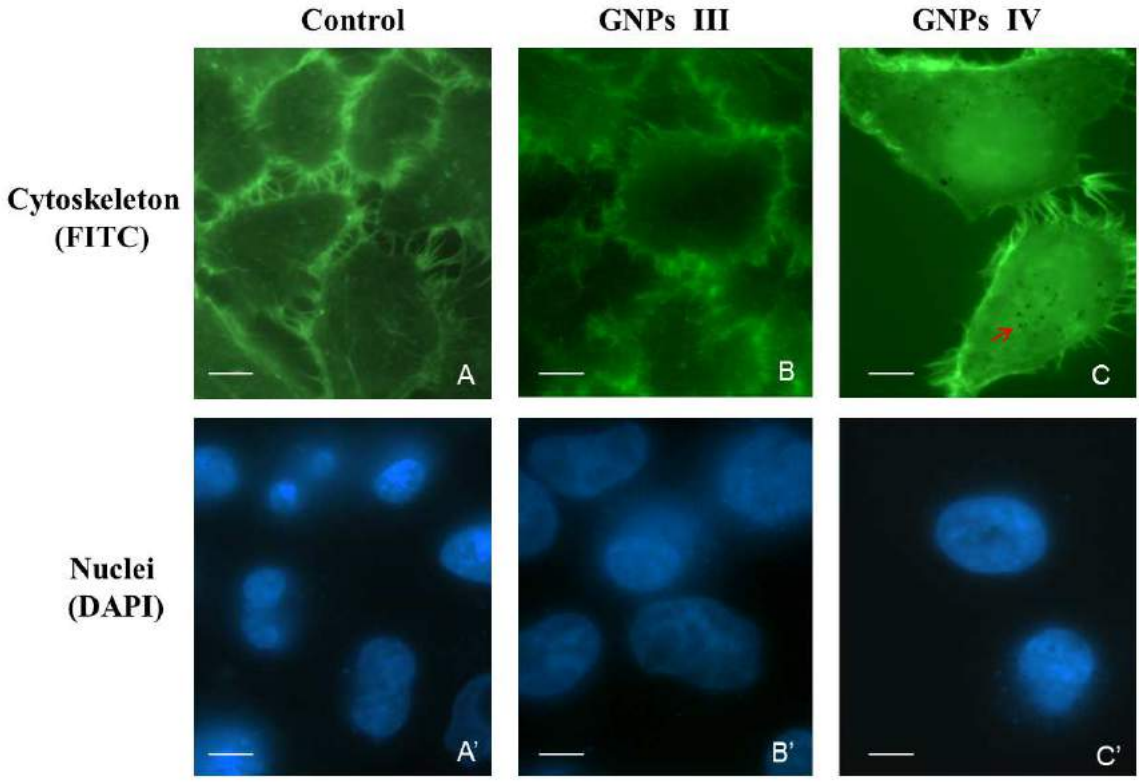

Figure 5.2.7: Effect of GNPs III and IV on the cytoskeleton of HeLa cells. The control cells were unexposed to GNPs (A, A'). The GNPs were placed in monolayer cells for 1h (B-C and B'-C'). The arrows indicate the GNPs aggregates in the cells. Scale bar is 10μm.

cytoskeleton in the F-Actin microfilaments. Cytoskeleton analysis was carried out by using the FITC-phalloidin to label the cytoskeleton (F-Actin microfilaments) and DAPI for the nucleus, figures 5.2.6 and 5.2.7. We observed that GNPs internalization was very efficient for the GNPs II-IV compared with the GNPs I; huge aggregates of GNPs can be observed at naked eye, almost all the aggregates were localized in the cytosol and close to the nucleus (Figs. 5.2.7 and 5.2.4). It seems that BSA improves the internationalization and the biocompatibility since more of these aggregates were observed for the GNPs IV. A visual analysis of the fluorescence microscopy images shown that the microfilaments not suffered any damage by the presence of the GNPs I-IV; the filaments seem well

formed and the adhesion of cells seems normal, such as control cells. The monolayers followed a normal growth; we did not see inhibition of cell proliferation or changes in cell morphology caused by the presence of the GNPs.

Discussion

Nanotoxicology as a new discipline dedicated to the suitable development and safety information related with the use of new materials in the order of nanometers size. Toxicology and genotoxicology studies are the basis for protection of human health and the environment relating to nanotechnology [56]. The in vitro toxicological studies become extremely relevant and important to characterize GNPs effects, and determine the safety parameters under which NPs can be useful for biomedical applications, before they can be tested in animal models. Currently, GNPs applications as therapeutic vehicles, as markers and in photothermal therapy are very promising; however, it is important to know about of all those possible consequences of their use. For example, some reports on the exposure of GNPs to different cell lines showed differential cytotoxicity as a function of NPs concentration, coating, size and roughness [52, 55, 56]. In this regard, here we focused the report on the toxicological study of gold nanoparticles coated with one inorganic compound and three organic molecules tested in HeLa Cells. The choice of HeLa cell as model system was based on the cell's physiological function, adherent phenotype and that form the continuous monolayer. The viability study was performed as parameter to comparative cytotoxicity assessment and the cellular responses to gold nanoparticles. Our study show promising results, first because cell viability not showed significantly differences with the control for all coatings, in fact the lowest measured value of viability was 90% for GNPs I in the monolayer cells (70% of confluence), our hypothesis for this low value is due to the presence of CTAB. Previous reports showed that porous silicon coated gold nanorods still exhibit a low degree of toxicity for the presence of CTAB, such as we observed. On the other hand, NPs coated with organic molecules shows better values of viability in both exposure cases **A)** and **B)**. In contrast with our result, a report

of a comparative study of gold nanoparticles on human endothelial cells, shown differential cytotoxicity depending of the concentration, coating, size and roughness of NPs [22, 52, 57]. Also metabolic activity was carried out and showed good values mainly for the case of the sub cultivated cell, it means that not significant differences were founded with the control, while in the case of cell monolayer, case **B)**, again the lowest value was for gold nanorods. Besides, our preliminary results showed that the internalization is dependent of the surface chemistry (silica, 4-ATP, cysteamine and cysteamine-BSA), in our case NPs coated with 4-ATP and cysteamine (positive charge) did not show significant agglomeration, at least from the visual analysis of the optical microscopy images, however in the case of GNPs IV, the optical microscopy images showed huge aggregates in the cytosol, many of them located close to the nucleus, these results show that HeLa cell membrane is very sensitive to the gold nanoparticles surface chemistry. In previous reports a similar behavior has been observed, for example, Cho et al.[87] showed that the deposition of Au nanospheres on the surface of cancer cells was highly dependent on the sign of surface charges on the Au nanospheres; Goodman et al.[59] and Sultana et al.[57], found that cationic (ammonium functionalized) gold nanoparticles were more cytotoxic that the anionic (carboxilate functionalized), and proposed that the nanoparticles interact with the cells passively rather than by energy-dependent processes, as suggested by Tkachenko et al.[88]. In this work, the gold nanoparticles coated with free amino and combined with BSA shown the best NP internalization, cells still were viable with high metabolic activity similar to controls. Therefore, the type of surface coating can play an important role in the internalization and cytotoxicity of gold nanoparticles [59–63]. If NPs cause any cytotoxicity or genotoxicity, significant modifications happen in the cytoskeleton affecting all the cellular functions i.e. proliferation, transport, adhesion, morphology, etc. [89]; in our case, the optical microscopy images (see figures 5.2.6 and 5.2.7) not show any biological change that affected the HeLa cells due to the exposing to gold nanoparticles, the acting filaments were intact, cell adhesion seems good and the kinetic growth also shows a normal behavior. Moreover, the metabolic activity of the

HeLa cells exposed to gold nanoparticles indicated good mitochondrial functionality. In contrast, Pernodet et al.[60] observed F-actin disruption on human dermal fibroblasts treated with citrate-gold nanoparticles therefore the adhesion, proliferation and motility cell were decrease. Also, in our case, the analysis of the nuclei (unfragmentation) and genomic DNA (integrity) indicate no genotoxicity (undamaged DNA) by the interaction with GNPs I-IV, such as was reported by Singh et al.[61], where chromosomal fragmentation happened, DNA strand breakages, point mutations, oxidative DNA adducts and alterations in gene expression profiles have largely been assessed based on in vitro assays for the diverse group of nanomaterials studied. The reduced cell toxicity we observed with gold nanoparticles coated with organic-thiol molecules may be a promising for use the field of nanomedicine like in photothermal therapy, drug delivery and microscopy imaging (as markers).

5.3 Conclusions

The Ag decahedral NPs were functionalized with 4-ATP and BSA, since we wanted to study their interaction with HeLa cell cultures. Unfortunately we can't find a proper method to clean the colloidal solution, to extract all the non attached 4-ATP molecules and the synthesis residues, without compromising the colloidal stability, see section 5.1. Future work will be focus in solving these stability problems and the interaction with cells. Nevertheless, we were able to functionalize four different samples of Au NPs with three different molecules (4-ATP, cysteamine and BSA) and to study the interaction with cancer cells. In section 5.2.2, gold nanorods coated with porous silica (GNPs I) and spherical gold nanoparticles were prepared, by using sodium borohydride as a reducer and functionalized during the synthesis with 4-aminothiophenol (GNPs II) and cysteamine (GNPs III), also BSA coated the functionalized GNPs III (GNPs IV) to increase the biocompatibility and colloidal stability of them, to study the toxicity of the functionalized NPs on HeLa cells. Our results showed that the functionalized NPs ex-

hibited excellent water dispersibility, low aggregation and good biocompatibility as Hela cells exposed to GNPs shows good viability in all the cases and high metabolic activity just like the controls, except in the case of gold nanorods due to the presence of CTAB. Furthermore, the fluorescence images of the cytoskeleton indicated the cellular uptake of gold nanoparticles localized in the cytosol and close to the nucleus, also no visible damages of F-actin microfilaments were observed. Our gold nanoparticles may be useful in fields like nanoimmunology, nanomedicine and nanobiotechnology.

CHAPTER 6

General Conclusions

This thesis presents the synthesis of silver and gold NPs, their functionalization with organic molecules aimed to evaluate their cytotoxicity in a cancer cell culture line.

In Chapters 3 and 4, an exhaustive study on the photochemical synthesis of silver NPs was presented. The synthesis of stable silver decahedral nanoparticles produced under blue LED irradiation of silver precursor solutions is reported in Chapter 3; the photochemical synthesis of silver nanoparticles by monitoring the concentration of amino acids and surfactants, the irradiance and the solution temperature was systematically studied. We used three amino acids and the results showed that L-arginine and L-lysine are best suited for improving the yield of decahedrons, 60 and 63% decahedral particles respectively. Meanwhile, the decahedron yield was lower for L-histidine (15%). The kinetics of the photochemical synthesis under different irradiations of 80, 50 and 15mW/cm^2 was followed, a two-fold reduction in the time of synthesis was obtained for the maximum irradiance. We were able to improve the decahedral formation when the photochemical synthesis was performed at 46^{o}C, obtaining 75% when PVP was used

as surfactant. When performing the photochemical synthesis using Triton X-100 as surfactant the decahedral nanoparticle formation was not observed at room temperature but was found to be 56% formation at 46^{o}C.

In later experiments, it was noted that the resulting plasmon band is highly influenced by the wavelength chosen to induce the photochemical transformation: blue light produced twin particles, such as decahedral, prisms, and bi-pyramidal nanoparticles, while green light allowed the formation of flat rounded particles. Moreover, the UV–Vis optical extinction spectra revealed different growth kinetics of nanoparticles during the photochemical synthesis; the differences on the plasmon bands in samples synthesized with blue and green LEDs opened the possibility of tuning the optical properties and controlling the morphology of silver particles by combining two light sources as the photochemical transformation happens. We made a study in which the photochemical synthesis of silver NPs was carried out by changing from blue to green radiation at different exposure times. The results showed the high tuning capability of the IPD-SPR band of silver nanoparticles, which results in different NP morphologies through the photochemical transformation of silver precursor solutions, these results are presented in Chapter 4. By means of a simple one-pot, two-step light assisted process, it was possible to transform small spheres in the precursor solutions into flat rounded, flat elongated, twin disks, and decahedral NPs. In addition, photochemical transformation with the use of two light sources, blue and green LEDs, allowed us to select the IPD-SPR band with high tuning accuracy, from 511 to 594nm, by simply controlling blue irradiation time. Besides, we showed some preliminary results of two promising applications of the photochemical produced Ag NPs. The first of them is the use of Ag decahedral NPs as a SERS substrate; by a simple solution-mixing and drop-casting method it was possible to detect a 1x10^{-7}M concentration of 4-ATP, this is a concentration four orders magnitude less than the detected by normal Raman spectroscopy. In the second possible application, we showed that the flat rounded and the rounded decahedral NPs can be deposited into a glass-ITO substrates for their use in organic photovoltaics. The potochemical method of synthesis of silver NPs presented

here could be escalated to farther regions of the IR with the use of longer wavelength light sources or in multistep procedures.

Chapter 5 presented the work done in the functionalization of silver decahedral and gold nanoparticles. Silver decahedral NPs were functionalized with 4-ATP and BSA, since we wanted to study their interaction with HeLa cell cultures. Unfortunately we can't find a proper method to clean the colloidal solution, to extract all the non attached 4-ATP molecules and the synthesis residues, without compromising the colloidal stability, see section 5.1. Future work will be focus in solving these stability problems and the interaction with cells. Nevertheless, we were able to functionalize four different samples of Au NPs with three different molecules (4-ATP, cysteamine and BSA) and to study the interaction with cancer cells. In section 5.2, gold nanorods coated with porous silica (GNPs I) and spherical gold nanoparticles were functionalized during the synthesis with 4-aminothiophenol (GNPs II) and cysteamine (GNPs III), also BSA coated the functionalized GNPs III (GNPs IV) to increase the biocompatibility and colloidal stability. These four gold NPs were incubated in HeLa cell cultures, our results showed that the functionalized NPs exhibited excellent water dispersibility, low aggregation and good biocompatibility as HeLa cells exposed to GNPs shows good viability in all the cases and high metabolic activity just like the controls, except in the case of gold nanorods due to the presence of CTAB. Furthermore, the fluorescence images of the cytoskeleton indicated the cellular uptake of gold nanoparticles localized in the cytosol and close to the nucleus, also no visible damages of F-actin microfilaments were observed. These gold nanoparticles may be useful in fields like nanoimmunology, nanomedicine and nanobiotechnology.

This thesis showed the potential of the photochemical method for the synthesis of silver NPs as a fast and low cost method that allows tuning the IPD-SPR band within a wide region of the visible spectrum. It was also presented a very simple method for the functionalization of gold NPs; these functionalized NPs were biocompatible with HeLa cell cultures since the cells did not showed any sign of toxicity.

APPENDIX A

Publications

During the time I was doing the PhD in CIO it was possible to publish the works that are listed next. The first two works, on the photochemical synthesis of silver NPs, are an integral part of this thesis and the base for the PhD project. Meanwhile, the other three publications were product of the collaborations in the Dr. Pichardo's Lab.

1. **P.E. Cardoso-Avila**, J.L. Pichardo-Molina, K. Upendra Kumar and J.A. Arenas-Alatorre (2014) Temperature and amino acid-assisted size- and morphology-controlled photochemical synthesis of silver decahedral nanoparticles, Journal of Experimental Nanoscience, 9:6, 639-651, DOI:10.1080/17458080.2012.683535

2. **P.E. Cardoso-Avila**, J.L. Pichardo-Molina, C. Murali Krishna and R. Castro-Beltran (2015) Photochemical transformation of silver nanoparticles by combining blue and green irradiation, J Nanopart Res, 17:160, DOI:10.1007/s11051-015-2920-x

3. P.G. Martinez-Torres, M.M.Martinez-Garcia, **P.E. Cardoso-Avila** and J.L. Pichardo-

Molina (2015) Facile Nanostructured Substrate Preparation Using Gold Nanocuboids for SERS, Nanomater Nanotechnol, 5:12, DOI:10.5772/60500

4. M.M. Martinez-Garcia, **P.E. Cardoso-Avila** and J.L. Pichardo-Molina (2016) Concave gold nanocubes on Al-6063 alloy as a simple and efficient SERS substrate, Colloids and Surfaces A: Physicochemical and Engineering Aspects, 493: 66-73, DOI:10.1016/j.colsurfa.2016.01.030

5. L. Rocha Osornio, **P.E. Cardoso Avila** y J.L. Pichardo Molina (2011), La espectroscopia Raman una herramienta útil en el análisis de materiales biológicos. In book: Aplicaciones de la Espectroscopia Raman en la Caracterización de Materiales, Publisher: Casa Editorial Innovación Editorial Lagares de México SA de CV, Editors: S. J. Jiménez Sandoval, L. Escobar Alarcón, M. A. Camacho López. Pág. 159.

Bibliography

[1] G Mie. Beiträge zur optik trüber medien, speziell kolloidaler metallösungen. *Ann Phy*, 330(3):377–445, 1908.

[2] CF Bohren and DR Huffman. *Absorption and scattering of light by small particles*. Wiley-Interscience, 1st edition, 1983.

[3] C Noguez. Surface plasmons on metal nanoparticles: the influence of shape and physical environment. *J. Phys. Chem. C*, 111(10):3806–3819, 2007.

[4] B Nikoobakht and MA El-Sayed. Preparation and growth mechanism of gold nanorods (nrs) using seed-mediatedgrowth method. *Chem. Mater.*, 15(10):1957–1962, 2003.

[5] AL González and C Noguez. Optical properties of silver nanoparticles. *phys. stat. sol. (c)*, 4(11):4118–4126, 2007.

[6] KJ Prashant, KS Lee, IH El-Sayed, and MA El-Sayed. Calculated absorption and scattering properties of gold nanoparticles of different size, shape, and composition: Applications in biological imaging and biomedicine. *J. Phys. Chem. B*, 110(14): 7238–7248, 2006.

[7] IO Sosa, C Noguez, and RG Barrera. Optical properties of metal nanoparticles with arbitrary shapes. *J. Phys. Chem. B*, 107(26):6269–6275, 2003.

[8] C Wu and Q Xu. Stable and functionable mesoporous silica-coated gold nanorods as sensitive localized surface plasmon resonance (lspr) nanosensors. *Langmuir*, 25 (16):9441–9446, 2009.

[9] MB Cortie and AM McDonagh. Synthesis and optical properties of hybrid and alloy plasmonic nanoparticles. *Chem. Rev.*, 111(6):3713–3735, 2011.

[10] CJ De Santis, AA Peverly, DG Peters, and SE Skrabalak. Octopods versus concave nanocrystals: Control of morphology by manipulating the kinetics of seeded growth via co-reduction. *Nano Lett.*, 11(5):2164–2168, 2011.

[11] S Kumar, N Harrison, R Richards-Kortum, and K Sokolov. Plasmonic nanosensors for imaging intracellular biomarkers in live cells. *Nano Lett.*, 7(5):1338–1343, 2007.

[12] A Radi, D Pradhan, Y Sohn, and KT Leung. Nanoscale shape and size control of cubic, cuboctahedral, and octahedral cu-cu_2o core-shell nanoparticles on si(100) by one-step, templateless, capping-agent-free electro-deposition. *ACS Nano*, 4(3): 1553–1560, 2010.

[13] M Rycenga, CM Cobley, J Zeng, W Li, CH Moran, Q Zhang, D Qin, and Y Xia. Controlling the synthesis and assembly of silver nanostructures for plasmonic applications. *Chem. Rev.*, 111(6):3669–3712, 2011.

[14] B Wiley, T Herricks, Y Sun, and Y Xia. Polyol synthesis of silver nanoparticles: Use of chloride and oxygen to promote the formation of single-crystal, truncated cubes and tetrahedrons. *Nano Lett.*, 4(9):1733–1739, 2004.

[15] Y Yang, Y Yan, W Wang, and J Li. Precise size control of hydrophobic gold nanoparticles using cooperative effect of refluxing ripening and seeding growth. *Nanotechnology*, 19(17):1—-10, 2008.

[16] J Zhang, MR Langille, ML Personick, K Zhang, S Li, and CA Mirkin. Concave cubic gold nanocrystals with high-index facets. *J. Am. Chem. Soc.*, 132(40):14012–14014, 2010.

[17] J Kimling, M Maier, B Okenve, V Kotaidis, H Ballot, and A Plech. Turkevich method for gold nanoparticle synthesis revisited. *J. Phys. Chem. B*, 110(32):15700–15707, 2006.

[18] J Turkevich, G Garton, and PC Stevenson. The color of colloidal gold. *J. Colloid Sci*, 9(1):26–35, 1954.

[19] J Turkevich, PC Stevenson, and J Hillier. A study of the nucleation and growth processes in the synthesis of colloidal gold. *Discuss. Faraday Soc.*, 11:55–75, 1951.

[20] A Henglein and M Giersig. Formation of colloidal silver nanoparticles: Capping action of citrate. *J. Phys. Chem. B*, 103(44):9533–9539, 1999.

[21] ML Personick and CA Mirkin. Making sense of the mayhem behind shape control in the synthesis of gold nanoparticles. *J. Am. Chem. Soc.*, 135(49):18238–18247, 2013. doi: 10.1021/ja408645b.

[22] P M Favi, M Gao, L J Sepulveda-Arango, S P Ospina, M Morales, J J Pavon, and T J Webster. Shape and surface effects on the cytotoxicity of nanoparticles: Gold nanospheres versus gold nanostars. *Journal of Biomedical Materials Research*, 2015. doi: 10.1002/jbm.a.35491.

[23] L Vigderman and ER Zubarev. High-yield synthesis of gold nanorods with longitudinal spr peak greater than 1200 nm using hydroquinone as a reducing agent. *Chem. Mater.*, 25(8):1450–1457, 2013.

[24] NR Jana, L Gearheart, and CJ Murphy. Wet chemical synthesis of silver nanorods and nanowires of controllable aspect ratio. *Chem. Comm.*, 7:617–618, 2001.

[25] DM Ledwith, AM Whelan, and JM Kelly. A rapid, straight-forward method for controlling the morphology of stable silver nanoparticles. *J. Mat. Chem.*, 17:2459–2464, 2007.

[26] X Dong, X Ji, H Wu, L Zhao, J Li, and W Yang. Shape control of silver nanoparticles by stepwise citrate reduction. *J. Phys. Chem. C*, 113(16):6573–6576, 2009.

[27] X Dong, X Ji, J Jing, M Li, J Li, and W Yang. Synthesis of triangular silver nanoprisms by stepwise reduction of sodium borohydride and trisodium citrate. *J. Phys. Chem. C*, 114(5):2070–2074, 2010.

[28] X Zheng, W Xu, C Corredor, S Xu, J An, B Zhao, and JR Lombardi. Laser-induced growth of monodisperse silver nanoparticles with tunable surface plasmon resonance properties and a wavelength self-limiting effect. *J. Phys. Chem. C*, 111 (41):14962–14967, 2007.

[29] KG Stamplecoskie and JC Scaiano. Light emitting diode irradiation can control the morphology and optical properties of silver nanoparticles. *J. Am. Chem. Soc.*, 132 (6):1825–1827, 2010.

[30] HH Huang, XP Ni, GL Loy, CH Chew, KL Tan, FC Loh, JF Deng, and GQ Xu. Photochemical formation of silver nanoparticles in poly(n-vinylpyrrolidone). *Langmuir*, 12(4):909–912, 1996.

[31] GV Krylova, AM Eremenko, NP Smirnova, and S Eustis. Photochemical preparation of nanoparticles of ag in aqueous-alcoholic solutions and on the surface of mesoporous silica. *Theoret Exp Chem*, 41(2):105–110, 2005.

[32] M Sakamoto, M Fujistuka, and T Majima. Light as a construction tool of metal nanoparticles: synthesis and mechanism. *J Photochem Photobiol B*, 20(1):33–56, 2009.

[33] B Pietrobon and V Kitaev. Photochemical synthesis of monodisperse size-controlled silver decahedral nanoparticles and their remarkable optical properties. *Chem. Mater.*, 20(16):5186–5190, 2008.

[34] H Lu, H Zhang, X Yu, S Zeng, KT Yong, and HP Ho. Seed-mediated plasmon-driven regrowth of silver nanodecahedrons (nds). *Plasmonics*, 7(1):167–173, 2012.

[35] H Wang, X Zheng, and J Chen. Transformation from silver nanoprisms to nanodecahedra in a temperature-controlled photomediated synthesis. *J Phys Chem C*, 116 (45):24268–24273, 2012.

[36] LC Yang, YS Lai, CM Tsai, YT Kong, CI Lee, and CL Huang. One-pot synthesis of monodispersed silver nanodecahedra with optimal sers activities using seedless photo-assisted citrate reduction method. *J Phys Chem C*, 116(45):24292–24300, 2012.

[37] MD Bordenavea, AF Scarpettinia, MV Roldánb, N Pellegrib, and AV Bragasa. Plasmon induced photochemical synthesis of silver triangular prisms and pentagonal bipyramids by illumination with light emitting diodes. *Mater Chem Phys*, 139(19): 100–106, 2013.

[38] PE Cardoso-Avila, JL Pichardo-Molina, K Upendra-Kumar, and JA Arenas-Alatorre. Temperature and amino acid-assisted size- and morphology-controlled photochemical synthesis of silver decahedral nanoparticles. *J Exp Nanosci*, 9(6): 639–651, 2014.

[39] RC Jin, YW Cao, CA Mirkin, KL Kelly, GC Schatz, and JG Zheng. Photoinduced conversion of silver nanospheres to nanoprisms. *Science*, 294(5548):1901–1903, 2001.

[40] B Tang, S Xu, X Hou, J Li, L Sun, W Xu, and X Wang. Shape evolution of silver nanoplates through heating and photoinduction. *ACS Appl Mater Interfaces*, 5(3): 646–653, 2013.

[41] J Zhang, MR Langille, and CA Mirkin. Synthesis of silver nanorods by low energy excitation of spherical plasmonic seeds. *Nano Lett*, 11(6):2495–2498, 2011.

[42] B Pietrobon, M McEachran, and V Kitaev. Synthesis of size-controlled faceted pentagonal silver nanorods with tunable plasmonic properties and self-assembly of these nanorods. *ACS Nano*, 3(1):21–26, 2009.

[43] M Maillard, Huang. P, and L Brus. Silver nanodisk growth by surface plasmon enhanced photoreduction of adsorbed [ag+]. *Nano Lett*, 3(11):1611–1615, 2003.

[44] PE Cardoso-Avila, JL Pichardo-Molina, C Murali-Krishna, and R Castro-Beltran. Photochemical transformation of silver nanoparticles by combining blue and green irradiation. *J Nanopart Res*, 17(3):10, 2015. doi: 10.1007/s11051-015-2920-x.

[45] AJ Machulek, HPM de Oliveira, and MH Gehlen. Preparation of silver nanoprisms using poly(n-vinyl-2-pyrrolidone) as a colloid-stabilizing agent and the effect of silver nanoparticles on the photophysical properties of cationic dyes. *Photochem. Photobiol. Sci.*, 2(9):921–925, 2003.

[46] TCR Rocha, H Winnischofer, E Westphal, and D Zanchet. Formation kinetics of silver triangular nanoplates. *J. Phys. Chem. C*, 7(111):2885–2891, 2007.

[47] Y Sun, B Mayers, and Y Xia. Transformation of silver nanospheres into nanobelts and triangular nanoplates through a thermal process. *Nano Lett.*, 3(5):675–679, 2003.

[48] Y Zhou, Y Kong, S Kundu, JD Cirillo, and H Liang. Antibacterial activities of gold and silver nanoparticles against escherichia coli and bacillus calmette-guérin. *Journal of Nanobiotechnology*, 2012(10):19, 2012.

[49] W Zhou, X Liu, and J Ji. More efficient nir photothermal therapeutic effect from intracellular heating modality than extracellular heating modality: an in vitro study. *J Nanopart Res*, 2012(14):1128, 2012.

[50] M Schomaker, D Heinemann, S Kalies, S Willenbrock, S Wagner, I Nolte, T Ripken, HM Escobar, H Meyer, and A Heisterkamp. Characterization of nanoparticle mediated laser transfection by femtosecond laser pulses for applications in molecular medicine. *Journal of Nanobiotechnology*, 2015(13):10, 2015.

[51] VP Pattani, J Shah, A Atalis, A Sharma, and JW Tunnell. Role of apoptosis and necrosis in cell death induced by nanoparticle-mediated photothermal therapy. *J Nanopart Res.*, 2015(17):20, 2015.

[52] N Lewinski, C Vicki, and R Drezek. Cytotoxicity of nanoparticles. *Small*, 4(1): 26–49, 2008.

[53] E Connor, J Mwamuka, A Gole, C Murphy, and M Wyatt. Gold nanoparticles are taken up by human cells but do not cause acute cytotoxicity. *Small*, 1:325–327, 2005.

[54] AM Alkilany and CJ Murphy. Toxicity and cellular uptake of gold nanoparticles: what we have learned so far? *J Nanopart Res*, 2010(12):2313–2333, 2010.

[55] N Khlebtsov and L Dykman. Biodistribution and toxicity of engineered gold nanoparticles: a review of in vitro and in vivo studies. *Chem. Soc. Rev.*, 40(3): 1647–1671, 2011.

[56] S Arora, J M Rajwade, and K M Paknikar. Nanotoxicology and in vitro studies: The need of the hour. *Toxicology and Applied Pharmacology*, 258(2):151–165, 2012.

[57] S Sultana, N Djaker, S Boca-Farcau, M Salerno, N Charnaux, S Astilean, H Hlawaty, and ML de la Chapelle. Comparative toxicity evaluation of flowershaped and spherical gold nanoparticles on human endothelial cells. *Nanotechnology*, 2015. doi: 10.1088/0957-4484/26/5/055101.

[58] IM Martinez-Paino, V Spolon-Marangoni, RdeC Silva de Oliveira, LM Greggi-Antunes, and V Zucolotto. Cyto and genotoxicity of gold nanoparticles in human

hepatocellular carcinoma and peripheral blood mononuclear cells. *Toxicology letters*, 2012(215):119–125, 2012.

[59] CM Goodman, CD McCusker, T Yilmaz, and V Rotello. Toxicity of gold nanoparticles functionalized with cationic and anionic side chains. *Bioconjug. Chem.*, 15(4): 897–900, 2004.

[60] N Pernodet, F Xiaohua, S Yuan, B Asya, R Aditi, J Sokolov, A Ulman, and M Rafailovich. Adverse effects of citrate/gold nanoparticles on human dermal fibroblasts. *Small*, 2(6):766–773, 2006.

[61] S Singh, V D'Britto, A A Prabhune, C V Ramana, A Dhawan, , and B L V Prasad. Cytotoxic and genotoxic assessment of glycolipid-reduced and -capped gold and silver nanoparticles. *New J. Chem.*, 34:294–301, 2010.

[62] X Liu, N Huang, H Wang, H Li, Q Jin, and Ji J. The effect of ligand composition on the in vivo fate of multidentate poly(ethylene glycol) modified gold nanoparticles. *Biomaterials*, 34:8370–8381, 2013.

[63] JJ Li, N Kawazoe, and G Chen. Gold nanoparticles with different charge and moiety induce differential cell response on mesenchymal stem cell osteogenesis. *Biomaterials*, 54:226–236, 2015.

[64] M Born and E Wolf. *Principles of Optics*. Cambridge University Press, 7th edition, 1999.

[65] A Lipson, HG Lipson, and H Lipson. *Optical Physics*. Cambridge University Press, 4th edition, 2010.

[66] A Smekal. Zur quantentheorie der dispersion. *Die Naturwissenschaften*, 5(11):873–875, 1923.

[67] PJ Larkin. *IR and Raman spectroscopy. Principles and spectral interpretation*. Elsevier, 1st edition, 2011.

[68] PN Prasad. *Nanophotonics*. Wiley Interscience, John Wiley and Sons, Inc., 1st edition, 2004.

[69] P Zijlstra, C Bullen, JWM Chon, and M Gu. High-temperature seedless synthesis of gold nanorods. *J. Phys. Chem. B*, 110(39):19315–19318, 2006.

[70] S Coskun, B Aksoy, and HE Unalan. Polyol synthesis of silver nanowires: An extensive parametric study. *Crystal. Growth Design*, 11(11):4963–5969, 2011.

[71] P Yu, J Huang, and J Tang. Observation of coalescence process of silver nanospheres during shape transformation to nanoprisms. *Nanoscale Res. Lett.*, 6(46):1–7, 2011.

[72] XC Jiang, WM Chen, CY Chen, SX Xiong, and AB Yu. Role of temperature in the growth of silver nanoparticles through a synergetic reduction approach. *Nanoscale Res. Lett.*, 6(1):32–40, 2011.

[73] X Liu, R Huang, and J Zhu. Functional faceted silver nano-hexapods: Synthesis, structure characterizations, and optical properties. *Chem. Mater.*, 20(1):192–197, 2008.

[74] G Wei, H Zhou, Z Liu, Y Song, L Wang, L Sun, and Z Li. One-step synthesis of silver nanoparticles, nanorods,and nanowires on the surface of dna network. *J. Phys. Chem. B*, 109(18):8738–8743, 2005.

[75] W Zhang, P Chen, Q Gao, Y Zhang, and Y Tang. High-concentration preparation of silver nanowires: Restraining in situ nitric acidic etching by steel-assisted polyol method. *Chem. Mater.*, 20(5):1699–1704, 2008.

[76] D Yu and VW-W Yam. Hydrothermal-induced assembly of colloidal silver spheres into various nanoparticles on the basis of htab-modified silver mirror reaction. *J. Phys. Chem. B*, 109(12):5497–5503, 2005.

[77] X Hu, T Wang, L Wang, and S Dong. Surface-enhanced raman scattering of 4-aminothiophenol self-assembled monolayers in sandwich structure with nanoparticle

shape dependence: off-surface plasmon resonance condition. *J. Phys. Chem. C.*, 111 (19):6962–6969, 2007.

[78] LS Taylor, FW Langkilde, and G Zografi. Fourier transform raman spectroscopic study of the interaction of water vapor with amorphous polymers. *Journal of Pharmaceutical Sciences*, 90(7):888–901, 2001.

[79] I Gorelikov and N Matsuura. Single-step coating of mesoporous silica on cetyltrimethyl ammonium bromide-capped nanoparticles. *Nano Lett.*, 8(1):369–373, 2007.

[80] S Silva, M Negri, M Henriques, R Oliveira, D W Williams, and J Azeredo. Adherence and biofilm formation of non-candida albicans candida species. *Trends Microbiol.*, 19(5):241–247, 2011.

[81] M C Chen and R C Lord. Laser-excited raman spectroscopy of biomolecules. viii. conformational study of bovine serum albumin. *J. Am. Chem. Soc.*, 98(4):990–992, 1976.

[82] A Kudelski and W Hill. Raman study on the structure of cysteamine monolayers on silver. *Langmuir*, 15(9):3162–3168, 1999.

[83] A Michota, A Kudelski, and J Bukowska. Influence of electrolytes on the structure of cysteamine monolayer on silver studied by surface-enhanced raman scattering. *J. Raman Spectrosc.*, 32(5):345–350, 2001.

[84] L Riauba, G Niaura, O Eicher-Lorka, and E Butkus. A study of cysteamine ionization in solution by raman spectroscopy and theoretical modeling. *J. Phys. Chem. A*, 110(50):13394–13404, 2006.

[85] K Kim, H B Lee, J-Y Choi, K L Kim, and K S Shin. Surface-enhanced raman scattering of 4-aminobenzenethiol in nanogaps between a planar ag substrate and pt nanoparticles. *J. Phys. Chem. C*, 115(27):13223–13231, 2011.

[86] K Kim, D Shin, J-Y Choi, K L Kim, and K S Shin. Surface-enhanced raman scattering characteristics of 4-aminobenzenethiol derivatives adsorbed on silver. *J. Phys. Chem. C.*, 115(50):24960–24966, 2011.

[87] E C Cho, J Xie, P A Wurm, and Y Xia. Understanding the role of surface charges in cellular adsorption versus internalization by selectively removing gold nanoparticles on the cell surface with a i2/ki etchant. *Nano Lett*, 9(3):1080–1084, 2009.

[88] AG Tkachenko, H Xie, Y Liu, D Coleman, J Ryan, W Glomm, M Shipton, S Franzen, and D Feldheim. Cellular trajectories of peptide-modified gold particle complexes: comparison of nuclear localization signals and peptide transduction domains. *Bioconjugate Chem.*, 15(3):482–490, 2004.

[89] E Fuchs and Y Yang. Crossroads on cytoskeletal highways. *Cell*, 98(5):547–550, 1999.